



Seamount Subduction Dynamics and Long-Term Evolution of the Franciscan Active Margin

G. Bonnet, F E Apen, M. Soret, J. Noël, B. Caron, Dia Ninkabou, Petr Zverev, D. Deldicque

► To cite this version:

G. Bonnet, F E Apen, M. Soret, J. Noël, B. Caron, et al.. Seamount Subduction Dynamics and Long-Term Evolution of the Franciscan Active Margin. *Tectonics*, 2024, 43 (3), pp.e2023TC008084. 10.1029/2023TC008084 . hal-04540559

HAL Id: hal-04540559

<https://hal.science/hal-04540559>

Submitted on 10 Apr 2024

HAL is a multi-disciplinary open access archive for the deposit and dissemination of scientific research documents, whether they are published or not. The documents may come from teaching and research institutions in France or abroad, or from public or private research centers.

L'archive ouverte pluridisciplinaire **HAL**, est destinée au dépôt et à la diffusion de documents scientifiques de niveau recherche, publiés ou non, émanant des établissements d'enseignement et de recherche français ou étrangers, des laboratoires publics ou privés.



Distributed under a Creative Commons Attribution - NonCommercial - NoDerivatives 4.0 International License

**Key Points:**

- The Snow Mountain Volcanic complex is a former hotspot volcano subducted to the seismogenic zone
- High-pressure fabrics and veins capture mixed brittle-ductile behavior of rocks and episodic fluid pulses in the seismogenic zone
- Thermal maturation of the subduction is achieved in ~10 My, subducting plate characteristics governs later accretion and arc activity

Supporting Information:

Supporting Information may be found in the online version of this article.

Correspondence to:

G. Bonnet,
gbonnet01@gmail.com









Citation:

Bonnet, G., Apen, F. E., Soret, M., Noël, J., Caron, B., Ninkabou, D., et al. (2024). Seamount subduction dynamics and long-term evolution of the Franciscan active margin. *Tectonics*, 43, e2023TC008084. <https://doi.org/10.1029/2023TC008084>

Received 4 SEP 2023

Accepted 25 FEB 2024

Seamount Subduction Dynamics and Long-Term Evolution of the Franciscan Active Margin

G. Bonnet^{1,2,3} , F. E. Apen^{3,4} , M. Soret⁵ , J. Noël⁶ , B. Caron² , D. Ninkabou² , P. Zverev² , and D. Deldicque⁵ 

¹Institute of Geological Sciences, University of Bern, Bern, Switzerland, ²CNRS-INSU, Institut des Sciences de la Terre de Paris, ISTE, Sorbonne Université, Paris, France, ³Department of Earth Science, University of California, Santa Barbara, CA, USA, ⁴Department of Geosciences, Princeton University, Princeton, NJ, USA, ⁵Laboratoire de Géologie, École Normale Supérieure, CNRS, UMR8538, Université PSL, Paris, France, ⁶OSU Ecce Terra, UAR 3455, Sorbonne Université, Paris, France

Abstract The Snow Mountain Volcanic Complex (SMVC; northern California, USA) is a well-preserved example of a coherently-exhumed subducted seamount. This study reappraises the genesis and evolution of this complex and surrounding units through detailed field, petro-structural and geochronological analyses. This work demonstrates that the SMVC (a) erupted at ~166 Ma as a hotspot volcano on the Farallon Plate, (b) entered the Franciscan subduction trench at ~118 Ma, and (c) was subsequently subducted to a depth of ~20 km (within the seismogenic zone), as shown by local blueschist-facies assemblages formed at 0.6 GPa, 240°C. Transient subduction interfaces are preserved above, within, and below the SMVC, making it an exceptional target to study seamount subduction dynamics. Like other seamounts, the subduction-related deformation was mainly accommodated along kilometer-scale internal thrust zones lubricated by serpentinite/metasediments, and within centimeter-thick crack-seal veins recording pulsed fluid flow near peak metamorphism. No unequivocal proof of seismic activity was found. The integration of other seamounts (some potentially belonging to a former seamount chain) in the Franciscan Complex suggests that exhumed seamounts are more abundant than previously thought. Moreover, pressure-temperature-time estimates of subduction metamorphism for the surrounding units, combined with previous work constrain the thermal maturation of the subduction zone through time and the in-sequence emplacement of the SMVC. Rapid changes in age of the subducted oceanic plate when subducted additionally hint to the subduction of large-offset transform faults on the former Farallon plate. Such a process might have been linked to changes in accretion dynamics and magmatic flare-ups in the arc.

1. Introduction

Seamount subduction has major effects on short-term (seconds to hundreds of years) and long-term (thousands of years to millions of years) subduction processes. At short timescales, subducted seamounts erupted on top of older oceanic plate (and more generally all kinds of seafloor highs) have been assumed to either increase or reduce seismogenic coupling. Increased seismogenic coupling implies that they might act as seismic asperities, owing to the concentration of elastic energy used to accommodate the deformation of the upper and lower subduction plates (Scholz & Small, 1997). Reduced seismogenic coupling could, however, be expected thanks to pervasive brittle deformation of the upper plate in response to seamount subduction (Wang & Bilek, 2011). Moreover, the seismological record and geophysical campaigns show that plate interfaces in the vicinity of subducted seamounts and seamount chains are commonly associated with long-term seismic quiescence, indicating that they may contribute to stopping seismic rupture propagation (hence limiting the potential magnitude of an earthquake; Kelleher & McCann, 1976; Lallemand et al., 2018). At geological timescales, seamount subduction may impact the geometry of subduction zones, including the frontal accretion versus underplating behavior, as well as subduction erosion, and magmatic gaps in volcanic arcs (Cloos & Shreve, 1996; Scholl & Von Huene, 2007; Wan et al., 2021). A better understanding of these processes requires imaging and extraction of tectonic and physical properties of subducted seamounts, which remain largely inaccessible by geophysical and seismological studies.

Seamounts in exhumed units from fossil subduction zones are generally dismembered and difficult to identify by other means than pillow basalts, bulk-rock geochemistry, and/or intercalation with carbonate sedimentary rocks (Barbero et al., 2021; Munoz-Montecinos et al., 2023; Tan et al., 2017). Among the best field examples of exhumed subducted seamounts with multi-kilometer-scale continuity, only a few have been extensively

© 2024. The Authors.

This is an open access article under the terms of the [Creative Commons Attribution-NonCommercial-NoDerivs License](#), which permits use and distribution in any medium, provided the original work is properly cited, the use is non-commercial and no modifications or adaptations are made.

documented, among which: (a) the Snow Mountain Volcanic Complex (SMVC) in the Franciscan Complex of California (MacPherson, 1983), (b) the Anarak unit in Central Iran (Bagheri & Stampfli, 2008), and (c) the Siah Kuh unit in southeastern Iran (Bonnet et al., 2020; Bonnet, Agard, Angiboust, Fournier, & Omrani, 2019; Bonnet, Agard, Angiboust, Monié, et al., 2019). Among these, the Anarak unit allowed to study the architecture of a seamount and subduction-related deformation in the upper plate (Bagheri & Stampfli, 2008). In comparison, the Siah Kuh unit allowed to study short-term subduction processes in subducted seamounts: a pseudotachylyte along an internal thrust zone records a small magnitude earthquake during subduction and numerous high-pressure veins point to pulses of high-fluid pressures favoring fluid circulation at depth (Bonnet, Agard, Angiboust, Fournier, & Omrani, 2019; Bonnet, Agard, Angiboust, Monié, et al., 2019). This unit is however singular as it formed as a forearc to an arc volcano that was later subducted (Bonnet et al., 2020). The relative scarcity of such units in the literature questions whether very specific, unit-dependent dynamics allow preservation from deep subduction or dismemberment.

This study focuses on the SMVC, which has dimensions comparable to the Siah Kuh unit, allowing direct comparison of structures and metamorphism. The likely genesis of the SMVC as a true hotspot volcano (MacPherson, 1983), and the presence of outcrops of the top and basal boundaries of the SMVC (presumably transient subduction interfaces), bring unique constraints on burial and decapitation mechanisms, from long-term to short-term. We here reappraise the structure and geochemical nature of the Snow Mountain Volcanic Complex and its surroundings. We provide new geochronological data for the timing of eruption and metamorphism of the SMVC and surrounding units to better understand the effects of seamount subduction on both short-term and long-term subduction processes. Additionally, the incorporation of a nappe-stack including the SMVC and surrounding units in the well-documented Franciscan paleo-subduction zone helps refining subduction evolution from juvenile to mature, emphasizing how the nature and diversity of the incoming plate affects erosion/accretion processes and arc magmatism at geological timescales.

2. Geological Context

The physical geography and geology of California are most impacted by its former location at the upper plate of subduction zone from the Early Jurassic to the Oligocene (Dickinson, 1970; Ernst, 1970). In eastern California, the Sierra Nevada is the main exposure of a magmatic arc. West of the Sierra Nevada, the Central Valley exposes a sedimentary basin (the Great Valley Group) formed in the forearc and then as a flexural basin of a former subduction zone (Ernst, 1970; Wakabayashi, 2015). Forearc sediments were deposited onto a forearc ophiolite, the Coast Range ophiolite (Arkula et al., 2023; Shervais et al., 2004). Below the ophiolite, remnants of the accretionary wedge crop out in the Franciscan complex that comprises most of the Coast Ranges of northern California (Figure 1). Whereas most of the Franciscan rocks record blueschist-facies conditions (Ernst, 1971), a small fraction are eclogite and amphibolite facies (e.g., Tsujimori et al., 2006; Wakabayashi, 1990). These higher-grade rocks crop out as coherent slabs at the roof of the Franciscan complex (e.g., Ward Creek, Willow Spring) or in mélange-like zones (e.g., Ring Mountain on the Tiburon Peninsula, Jenner) cropping out at multiple structural levels (Wakabayashi, 2015).

The area of the Snow Mountain Volcanic Complex in northern California (Figure 1) is one of the best locations to observe a near-continuous cross-section through the former accretionary wedge, assumed forearc ophiolite and forearc basin.

In this area, east-dipping Jurassic to Cretaceous Great Valley Group sediments crop out east of the Stonyford Volcanic Complex, separated by a steep east-dipping fault, possibly a former west-verging thrust fault (Brown, 1964; Shervais, Zoglman Schuman, & Hanan, 2005). The Stonyford Volcanic Complex is composed of a 7×3 km body of pillow and massive basalt, hyaloclastite, radiolarian chert and siliceous mudstone, interpreted as a relatively intact submarine volcano (Shervais, Zoglman Schuman, & Hanan, 2005; Shervais & Hanan, 1989). The lavas are dominantly oceanic tholeiite, with less abundant alkali basalt (generally found overlying the tholeiite in most places, and chemically comparable to hyaloclastite erupted near the top of the unit), and sub-ordinate intercalations of high-aluminum low-titanium basalts (Bailey & Blake, 1974; Shervais & Hanan, 1989; Shervais, Zoglman Schuman, & Hanan, 2005). The eruption age of the Stonyford Volcanic Complex is older than 165–163 Ma based on Ar-Ar dating of alkali basaltic glass, consistent with the Bajocian-Bathonian stratigraphic age for radiolarian chert interbedded within the lavas (Shervais, Murchey, et al., 2005). Whether the Stonyford Volcanic Complex belongs to the (mainly) supra-subduction-zone (SSZ) forearc Coast Range Ophiolite or to the

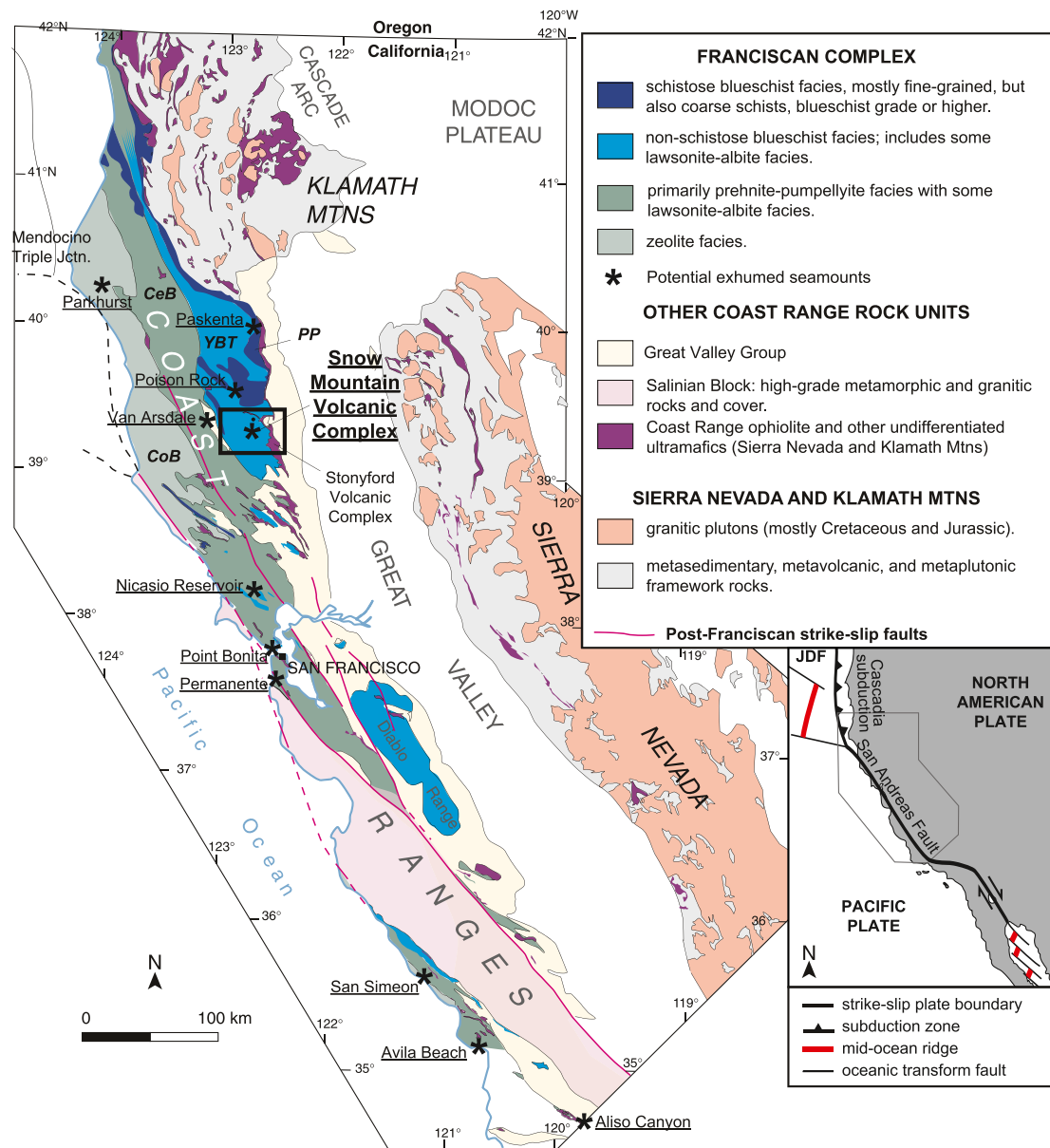


Figure 1. The Snow Mountain Volcanic Complex (black rectangle) in northern-central California and in the Franciscan Complex. Also underlined are the locations of other localities described as subducted seamounts in the Franciscan complex (either almost intact or strongly dismembered in shale-matrix mélangé units). Abbreviations: CeB, Central Belt; CoB, Coastal Belt; PP, Picket Peak terrane; YBT, Yolla Bolly Terrane. Modified from Wakabayashi (2017b). Inset: large-scale tectonic context of the area. JDF = Juan de Fuca plate.

Franciscan accretionary complex has been a matter of debate (Figure 1, Hopson & Pessagno, 2005; MacPherson & Phipps, 1985; Shervais & Kimbrough, 1985b). Its structural position ties it to the Coast Range ophiolite (Shervais, Zoglman Schuman, & Hanan, 2005), and radiolarian chert assemblages are of similar ages than other Coast Range ophiolite outcrops (yet more distal, Hopson & Pessagno, 2005).

The Stonyford Volcanic Complex is wrapped by strongly sheared serpentinite, which is semi-continuous along ~100 km of what is called the Tehama-Colusa Serpentinite Mélange (Hopson & Pessagno, 2005; hereafter abbreviated as TCSM; Figures 1 and 2). The TCSM contains blocks of ultramafic rocks (lherzolite and harzburgite) locally reaching 5 × 2 km in size, unmetamorphosed volcanogenic sediments, metasediments, greenstone and ultramafic to felsic igneous rocks and blueschist to amphibolite-facies mafic high-grade blocks (Choi et al., 2008; Huot & Maury, 2002; Shervais, Zoglman Schuman, & Hanan, 2005). Zircon U-Pb dates from

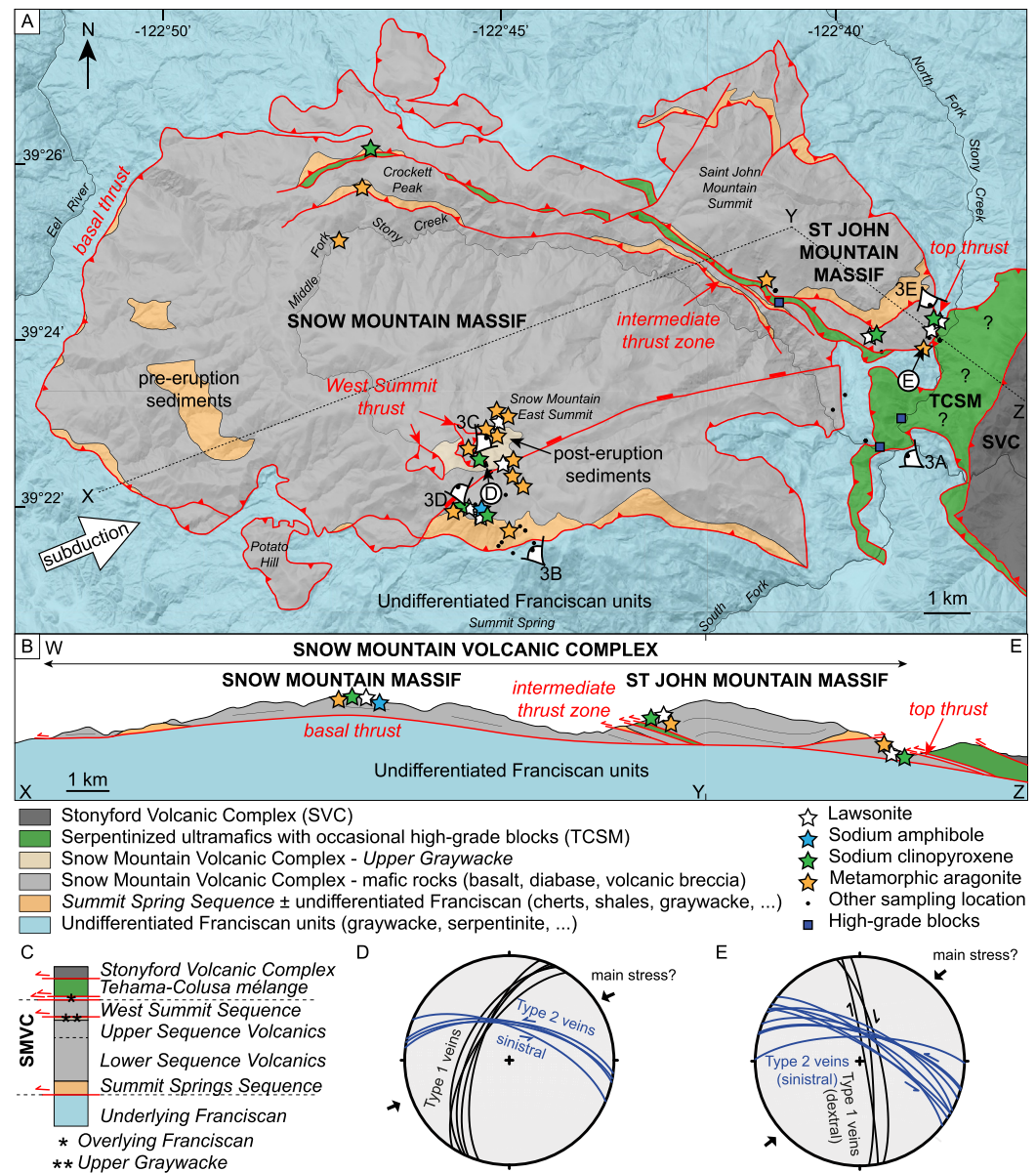


Figure 2. Map and structural data of the Snow Mountain Volcanic Complex (SMVC) and surroundings. (a) Lithological-metamorphic map, compiled from mapping by MacPherson (1983) and Shervais, Zoglman Schuman, and Hanan (2005), and new observations. “Eyes” and labels show the location of panoramas shown on Figures 3a–3c, dotted line shows the location of the cross-section along X-Y-Z, and circles show the location of structural measurements of panels (d and e). The geographical extent of the Summit Spring Sequence may be significantly smaller than mapped here and is discussed in text. Paleosubduction direction after Ring and Brandon (1994) (b) Cross-section along X-Y-Z. (c) Schematic tectonostratigraphic log of the Snow Mountain area. (d) Orientation of two main conjugated fracture populations (filled by quartz-plagioclase-lawsonite-bearing veins) in basalt close to the West Summit thrust. (e) Orientation of two main fracture populations (filled by quartz-aragonite-lawsonite-bearing veins) in basalt close to the top thrust.

intermediate to felsic igneous blocks in the serpentinite matrix at 165–163 Ma are compatible with the ages of the Stonyford Volcanic Complex (Shervais, Murchey, et al., 2005).

Undifferentiated Franciscan units below the SMVC are dominantly low-grade metagraywacke and metapelite, mapped as part of the Central Belt of the Coast Ranges (Dumitru et al., 2010). They also include radiolarian chert, metabasite and serpentinitized ultramafic rocks.

The Snow Mountain Volcanic Complex (Figure 2a) was first described as a seamount by MacPherson (1983). It comprises a deep-sea sedimentary base, the *Summit Spring Sequence* made of radiolarian chert, shale and graywacke. These rocks are locally intruded by diabase and overlain by mafic basaltic lavas (flows, pillows, pillow breccia) of the *Lower Sequence Volcanics*, thin chert layers in the *Upper Chert* and basaltic breccias and lava flows (in place with ropy, *pahoehoe*-type textures) in the *Upper Sequence Volcanics*. The *West Summit Sequence* (Figures 2a and 2b) is a thin unit of basaltic to rhyolitic volcanics thrust over the *Upper Sequence Volcanics* and *Upper Graywacke*. The edifice is affected by two internal thrust zones, the *West Summit thrust*, at the base of the *West Summit Sequence*, and the *intermediate thrust zone*, separating the massifs of Snow Mountain and Saint John Mountain. The whole SMVC is thrust over Franciscan units, composed mainly of graywacke, cherts, and serpentinite (Figures 2a and 2b). Lavas from the SMVC show a transitional to alkaline signature (MacPherson, 1983; Shervais & Kimbrough, 1987). This geochemical signature, together with the eruption of basalt on top of deep-sea sediments and subsurface to subaerial volcanic facies, led MacPherson (1983) to describe this unit as a seamount. The whole SMVC is affected by low-grade blueschist-facies metamorphism in a subduction context at mature thermal state (MacPherson, 1983).

3. Structural Observations and Sampling Strategy

Geological observations and sample collection were mainly performed in three areas of the Snow Mountain Volcanic Complex: (a) the Summit Spring to Snow Mountain summit area in the south, (b) the area west of Crockett Peak in the north, and (c) South of Saint John Mountain in the east (Figure 2). These areas were chosen for accessibility and representativity of the complex, because they respectively show: (a) underlying Franciscan units, *basal thrust* of the SMVC, *Summit Spring Sequence*, *Lower Sequence Volcanics*, *Upper Sequence Volcanics*, *Upper Graywacke*, *West Summit thrust*, and *West Summit Sequence* volcanics; (b) underlying Franciscan units, *Summit Spring Sequence*, *basal thrust*, *Lower Sequence Volcanics* and the *intermediate thrust zone* (separating the Snow Mountain and Saint John Mountain massifs); and (c) overlying Franciscan units, *top thrust*, *Lower Sequence Volcanics*, and *intermediate thrust zone*.

Figure 3 shows some of the main field relationships in the Snow Mountain area. The Snow Mountain area is at first sight a nappe stack of accretionary material, composed of a minimum of six thrust-delimited nappes. From bottom to top the nappes comprise (Figures 2a, 2b, and 3a): (a) undifferentiated Franciscan units, (b) Snow Mountain massif, (c) Saint John Mountain massif (both Snow Mountain and Saint John Mountain making the SMVC), (d) thin overlying Franciscan metasediments, (e) the TCSM and (f) volcanic sequence of the Stonyford Volcanic complex. The thrust at the base of the SMVC separates undifferentiated Franciscan units from SMVC basalt and chert (Figure 3b). Near the Snow Mountain twin summits, the *Upper Graywacke* lies unconformably upon basalt and chert from the *Lower* and *Upper Sequence Volcanics* (Figure 3c). The *Lower* and *Upper Sequence Volcanics* and the *Upper Graywacke* are thrust beneath the *West Summit Sequence* (Figure 3d). On the eastern slopes of the Saint John Mountain massif, east-dipping basaltic flows are thrust under phyllite and graywacke (along the *top thrust*), themselves overlain by the TCSM and the Stonyford Volcanic Complex (Figure 3e).

Volcanic rocks crop out throughout the SMVC, as pillow basalt and diabase sill or flow in the *Lower Sequence Volcanics* (Figure 3f). Peduncles in pillows of the *Lower Sequence Volcanics* indicate their upright position throughout the unit (Figures 3g and 3h).

Deformation in the SMVC is localized along thrust faults, such as the Snow Mountain basal thrust, where cataclastic basalt, shale, and chert were observed (Figure 3i), along with static carbonate mineralization, but also within the *intermediate thrust zone* and in the *West Summit thrust*, where sigmoidal fractures and drag folds in the foliation define a top to the southwest shear sense (Figure 2c). Sheared zones around faults are about or less than 10 m thick, except around the *West Summit thrust* where the sheared zone is ~50 m across.

Multiple generations of veins were observed in basalt and radiolarian chert (Figures 3j and 3k). Some generations have a preferred orientation, and the kinematics of their emplacement could be identified in some sites thanks to small displacements of other veins or emplacement after “en-échelon” veins. The majority of these vein arrays is compatible with NE-SW compression direction (Figures 2d and 2e; Figure S1 in Supporting Information S1). These veins usually contain white (quartz-dominated), cream-colored (lawsonite, or carbonate) and/or green (clinopyroxene) mineralization, among other minerals (see Section 7). Most do not have

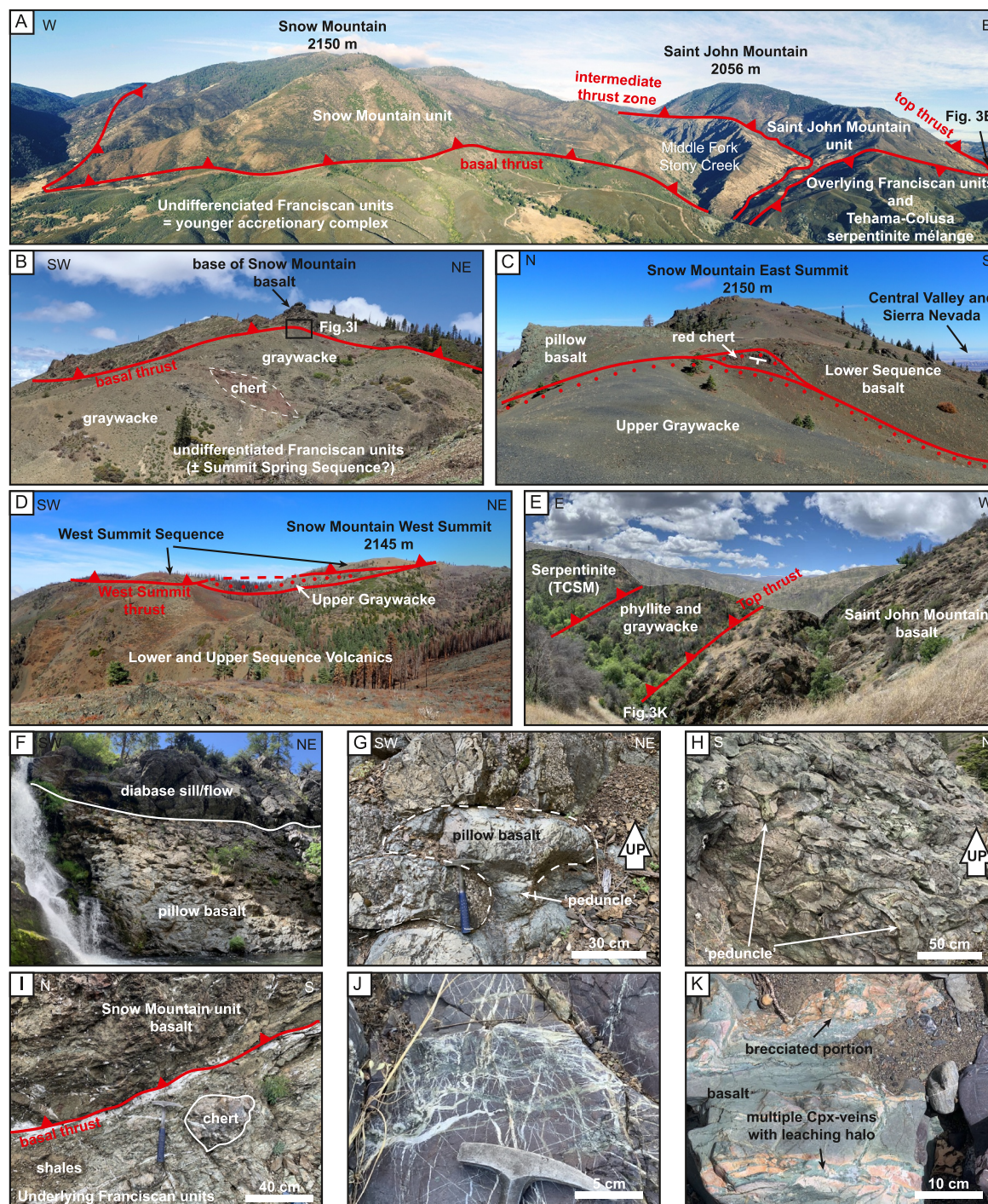


Figure 3. Field exposures. (a) Panoramic drone view of the contact between Snow Mountain and Saint John Mountain massifs. Notice the shift between the location of the incision of the Middle Fork of Stony Creek and the nearby thrust fault, suggesting ~600 m of erosion. (b) Basal contact of the Snow Mountain unit over undifferentiated Franciscan. (c) Top of the Snow Mountain massif and successive sedimentary contacts of red chert (directly on top of pillow basalt) and discordant sediments of the SMVC Upper Graywacke. (d) The West Summit Thrust, a minor thrust system atop of the Snow Mountain Massif. (e) Thrust sequence on top of the SMVC. (f) Pillow basalts overlain by diabase sill or flow in the North of Snow Mountain massif. (g) Normally oriented pillow basalt from the same outcrop. (h) Normally oriented pillow basalts from the South of Snow Mountain unit. (i) Tectonic breccia at the basal contact of the Snow Mountain unit with underlying Franciscan sedimentary rocks. Location of picture on panel (b). (j) Abundant metamorphic veins from the western part of the Saint John Mountain massif. (k) Pyroxene-bearing veins with leaching haloes and brecciated textures in the westernmost part of the Saint John Mountain unit. Location of picture on panel (e).

alteration haloes, except for those at the contact with the upper unit in the easternmost part of the Saint John Mountain massif (Figure 3k).

Franciscan units structurally below the SMVC consist of graywacke, chert (locally with preserved submillimeter radiolaria), and serpentinite/ophiocarbonate. The exact location of the contact between these units and the *Summit Spring Sequence* is not clear.

Units structurally above the SMVC were observed directly in contact with the SMVC on the eastern slopes of the Saint John Mountain in the streambed of the North Fork of Stony Creek. They consist of <100-m-thick sediments (shales and graywacke) overlain by serpentinite of the TCSM. The contact between the SMVC and overlying sediments is strongly sheared across about or less than 10 m, and consists of vein-rich basalts on one side and fine-grained (clay-rich) sediments on the other side. Roughly 50-m-thick intercalations of micaschists and graywacke were observed within the thrust zone between Snow Mountain and Saint John Mountain, again overlain by serpentinite. Decimeter-to-meter sized blocks of mafic metamorphic rocks are observed within these intercalated sediments and within serpentinite of the TCSM.

Sampling was done within the different volcanic and sedimentary sequences of the SMVC and surrounding units. A focus was on the most pristine and undeformed samples for magmatic geochemistry, on seemingly less pristine rocks and veins for metamorphic assemblages. Sample locations are shown on the map in Figure 2a.

4. Petrography and Deformation Textures

4.1. SMVC Volcanic Rocks

Mafic lavas from the Snow Mountain Volcanic Complex generally occur as pillows, with chilled margins, and a variable vesicularity (Figure 4a). Vesicles are empty or filled by calcite or silicate, particularly near pillow margins. Rare samples display macroscopic olivine partly altered to clay minerals (iddingsite; Figures 4b and 4c). Most samples have porphyritic textures, with augite phenocrysts and plagioclase microcrysts in a dark matrix of former volcanic glass and iron oxide (Figures 4d and 4e).

The West Summit rhyolite has a brecciated texture, with plagioclase and quartz in a dark matrix made of recrystallized glass, and rare ferro-magnesian minerals (Figure 4f).

Common alteration of the volcanic rocks is marked by abundant glass replacement by pumpellyite and chlorite, saussuritized and albitized plagioclase and of vesicles filled by secondary minerals such as carbonates, chlorite or pumpellyite (Figures 4a–4e).

4.2. SMVC Incipient High-Pressure Metamorphism and Deformation

Incipient metamorphism of the volcanic rocks is documented by the crystallization of mineral products, such as fine-grained green pyroxene and blue amphibole replacing plagioclase (Figures 4f and 4g), or more commonly aragonite, found filling vesicles (Figure 4h) or replacing former plagioclase. Most newly-formed minerals are, however, within veins in the mafic volcanics. Metamorphic veins are usually aragonite-calcite quartz (Figure 4i; aragonite appears with distinct interference colors and with finer twins compared to calcite and has been formally identified with Raman spectroscopy in every case), lawsonite-quartz, or clinopyroxene-lawsonite-albite-quartz (Figures 4j and 4k).

The imprint and style of deformation varies in the SMVC, depending on the lithology and proximity to thrust zones (see Figure S2 in Supporting Information S1). It consists of both brittle and plastic deformation. Vein opening is the main brittle feature affecting all kinds of rocks (basalt, chert, graywacke). Some samples show numerous vein opening events and crack-seal textures are common, locally marked by high-pressure mineral crystallization (Figures 4k and 4l). Quartz-carbonate-filled tensile fractures are also observed in fine-grained graywacke, roughly orthogonal to pressure-solution seams marking incipient plastic deformation (Figure 5a). The most deformed sediments along the *top thrust* have mylonitic fabrics, with pressure-solution seams along the foliation and recrystallized quartz porphyroclasts (Figure 5b). Folded veins also serve as a deformation marker (e.g., Figure 5c), and quartz recrystallization associated to grain size reduction is observed at the tails of boudinaged veins in pressure shadows. Quartz in veins within all lithologies shows bulging at grain boundaries (Figure 5d), undulose extinction and deformation lamellae of various thickness (Figure 5e). Aragonite is also locally twinned or affected by deformation lamellae (Figure 5f). Most basaltic rocks seem

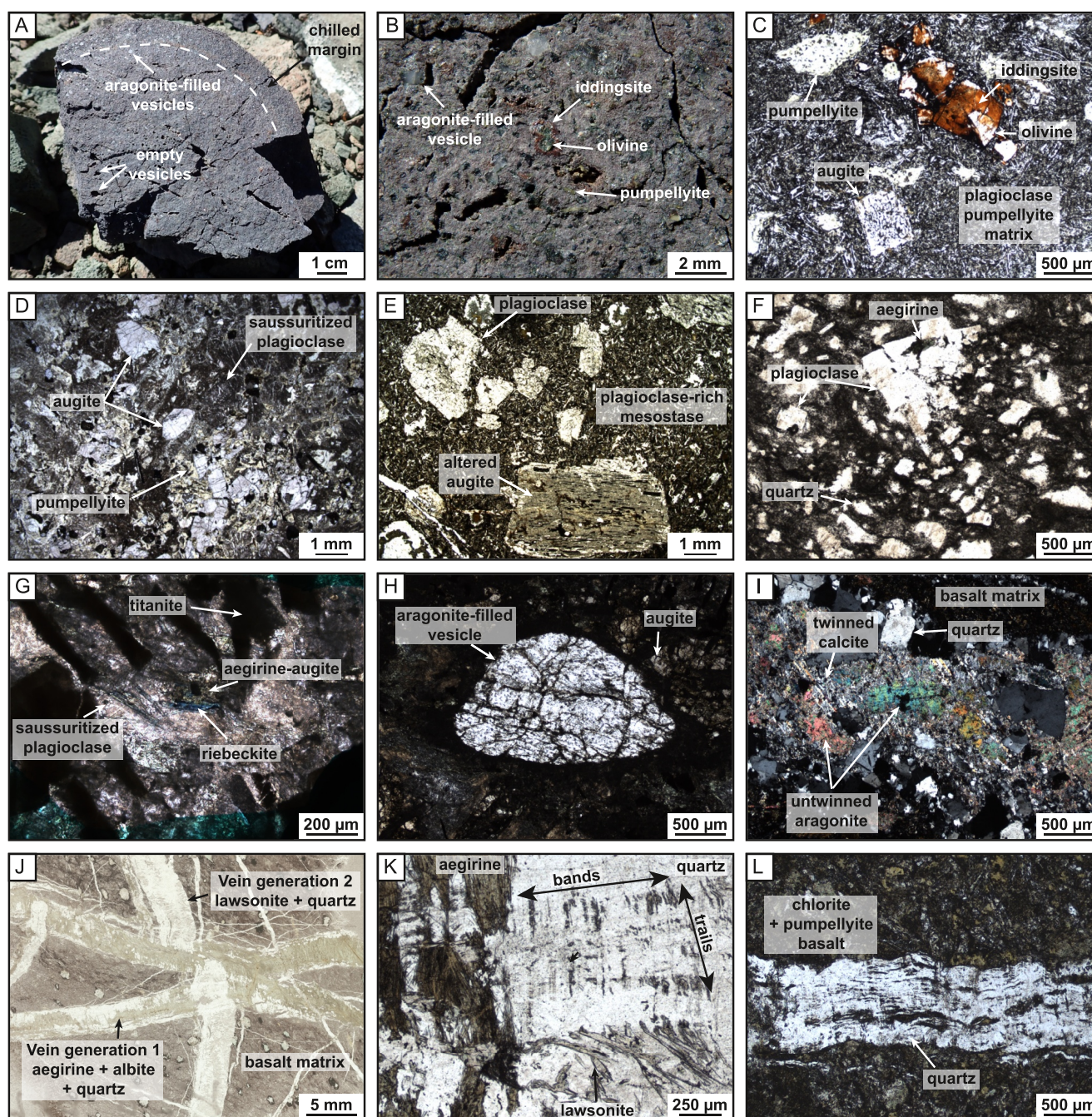


Figure 4. Petrography of the Snow Mountain Volcanic Complex and surroundings (1/2). (a) Portion of a vesicular pillow basalt from the top of the Snow Mountain unit (SM19-17), showing a melanocratic chilled margin with preferentially aragonite-filled vesicles. (b) Zoom on the same rock showing the occurrence of primary olivine crystals surrounded by secondary iddingsite. Secondary pumpellyite pseudomorphically replaces elongated crystals. (c) Microphotograph of the same rock, showing olivine altered to iddingsite, altered augite, in a pumpellyite-plagioclase matrix/mesostase. (d) Microphotograph of an altered diabase from the northwest SMVC (SM20-26, Figure 3f) with preserved millimeter-sized primary augite, strongly saussuritized plagioclase and secondary pumpellyite. (e) Microphotograph of well-preserved basaltic textures with augite and plagioclase megacrysts in a fine-grained plagioclase-rich mesostase (SM19-01; south SMVC). (f) Microphotograph of a rhyolitic assemblage with quartz and plagioclase and potentially metamorphic aegirine (SM20-11; Snow Mountain West Summit). (g) Microphotograph of an altered basalt with primary titanite, saussuritized plagioclase and metamorphic aegirine-augite and riebeckite (SM19-04; south SMVC). (h) Microphotograph of an aragonite-filled vesicle in the same sample SM19-04. (i) Microphotograph of a quartz-carbonate vein in a basalt (SM19-02; south SMVC), showing retrogression textures of aragonite (here untwinned) to calcite (here strongly twinned). (j) Thin-section scan (made with Keyence at Sorbonne Université) of a basaltic sample affected by at least two generations of metamorphic veins, the first containing aegirine-augite within two veins of distinct orientation, the second containing lawsonite. Post-vein 2 opening along vein 1 allowed some additional displacement (SM19-27; western base of the Saint John Massif). (k) Microphotograph of the same sample with the intersection of the two vein generations showing crack-seal textures, with lawsonite inclusion bands and inclusion trails in quartz. (l) Microphotograph of the same quartz-aragonite vein in basalt as (i), showing crack-seal inclusion bands marked by portions of the basaltic host.

undeformed, except in high strain domains along the *West Summit thrust* and the *top thrust* (Figure 5g). Foliation in basalt is marked by the alternation of flattened and partially dissolved pumpellyite-chlorite-quartz-filled vesicles and oxide-dominated levels, turning locally to a mylonitic fabric with sigmoidal-shaped pumpellyite porphyroclasts (Figure 5i). Subsequent brittle deformation is observed affecting this foliation along the *top thrust* (Figure 5j).

4.3. Franciscan High-Grade Blocks

Three high-grade mafic blocks with distinct paragenetic histories were sampled in the *intermediate thrust zone* (SM20-45-2) and in the serpentinite above Snow Mountain (SM20-03, SM20-67). Sample SM20-03 preserves augite and titanite porphyroblasts of magmatic origin, surrounded by oriented blue amphibole in association with pumpellyite (Figure 5j). The sample is cut by deformed jadeite and omphacite veins. Sample SM20-45-2 shows a more pronounced schistosity, with large amounts of strongly oriented green to pale blue amphibole associated with an omphacitic matrix, plagioclase and titanite (Figure 5k). The sample is crosscut by a late cm-thick plagioclase vein, associated with mm-scale displacement. In sample SM20-67, the matrix is made of foliated mm-scale brown hornblende crystals and (possibly magmatic) ilmenite. Hornblende crystals are statically overgrown by blue amphibole, rare omphacite and white mica, and chlorite (Figure 5l). Titanite is observed as dark overgrowths around ilmenite, and as pale crystals included in hornblende and along hornblende crystal boundaries.

5. Whole-Rock Geochemistry

Twenty-seven samples were analyzed for whole-rock major elements, trace elements and loss on ignition (LOI). A novel approach was used for the measurement of Pb isotopes using a triple quadrupole mass spectrometer. All analyses were done on the ALIPP6 platform at Sorbonne Université. Detailed procedures are available in Text S3 of Supporting Information S1. The whole SMVC and high-grade blocks sampled in the surrounding area were affected by hydrothermal alteration and high-grade metamorphism. In volcanic rocks, this is marked by the replacement of volcanic glass, and widespread chlorite and clay minerals replacing ferromagnesian minerals. LOI values from 1.4 to 15 wt.% also attest to intense hydration/carbonation of some rocks. To avoid bias linked to element mobilization during the alteration, samples with LOI above 10 wt.% are not shown below. Most discrimination diagrams used here (except possibly for the TAS diagram, see for example Bonnet et al. (2020)) involve relatively fluid-immobile elements.

5.1. Snow Mountain Mafic Rocks

Mafic rocks from the SMVC plot mainly in the picro-basalt, basanite-tephrite, basalt, trachy-basalt and basaltic trachy-andesite fields of the $\text{Na}_2\text{O} + \text{K}_2\text{O} - \text{SiO}_2$ (TAS) diagram and fall along an alkaline trend with strong enrichment in alkaline elements upon differentiation (Figure 6a). All samples plot between the basalt and alkali basalt fields of the $\text{Zr/Ti} - \text{Nb/Y}$ diagram (Figure 6b). Samples plot mainly within the OIB field of the $\text{V} - \text{Ti}$ diagram, with a few samples in the contiguous alkaline OIB and MORB fields (Figure 6c). All samples plot in the MORB-OIB array of the $\text{Th/Yb} - \text{Nb/Yb}$ diagram, clustered between E-MORB and OIB (Figure 6d). They also plot between E-MORB and (alkaline to tholeiitic) OIB on the $\text{TiO}_2/\text{Yb} - \text{Nb/Yb}$ diagram (Figure 6e), and between E-MORB and OIB in the $\text{Th} - \text{Hf} - \text{Ta}$ diagram (Figure 6f). Rare-earth element (REE) diagrams show an enrichment in light rare-earth elements (LREE) compared to chondrite (La concentrations from 40 to 143 times larger than chondrite), and a relative depletion in heavy REE (HREE) compared to LREE (Lu concentrations from 10 to 36 times larger than chondrite), and no distinct Eu anomaly (Figure 6g). Extended trace-element spider diagrams (normalized to primitive mantle) show similar trends for the REE, heterogeneity in the most fluid-mobile elements (Cs, Rb, Ba, U) as well as slightly positive Nb – Ta anomalies, distinct negative Sr anomalies and no Ti anomalies (Figure 6h). Values of $^{206}\text{Pb}/^{204}\text{Pb}_{167\text{ Ma}}$, $^{207}\text{Pb}/^{204}\text{Pb}_{167\text{ Ma}}$, and $^{208}\text{Pb}/^{204}\text{Pb}_{167\text{ Ma}}$ for sample SM20-40 are 18.464 ± 0.095 , 15.600 ± 0.078 and 38.122 ± 0.320 , overlapping with the depleted MORB mantle compositions (Figures 6k and 6l). Higher $^{206}\text{Pb}/^{204}\text{Pb}$ values for samples SM19-03 and SM20-27 (Figures 6k and 6l) are correlated with higher concentrations in Sr ($207\text{ }\mu\text{g.g}^{-1}$ and $187\text{ }\mu\text{g.g}^{-1}$, vs. $78\text{ }\mu\text{g.g}^{-1}$ in SM20-40), Ba ($432\text{ }\mu\text{g.g}^{-1}$ and $809\text{ }\mu\text{g.g}^{-1}$, vs. $56\text{ }\mu\text{g.g}^{-1}$ in SM20-40) and Rb ($16.79\text{ }\mu\text{g.g}^{-1}$ and $11.75\text{ }\mu\text{g.g}^{-1}$, vs. $5.42\text{ }\mu\text{g.g}^{-1}$ in SM20-40), suggesting alteration.

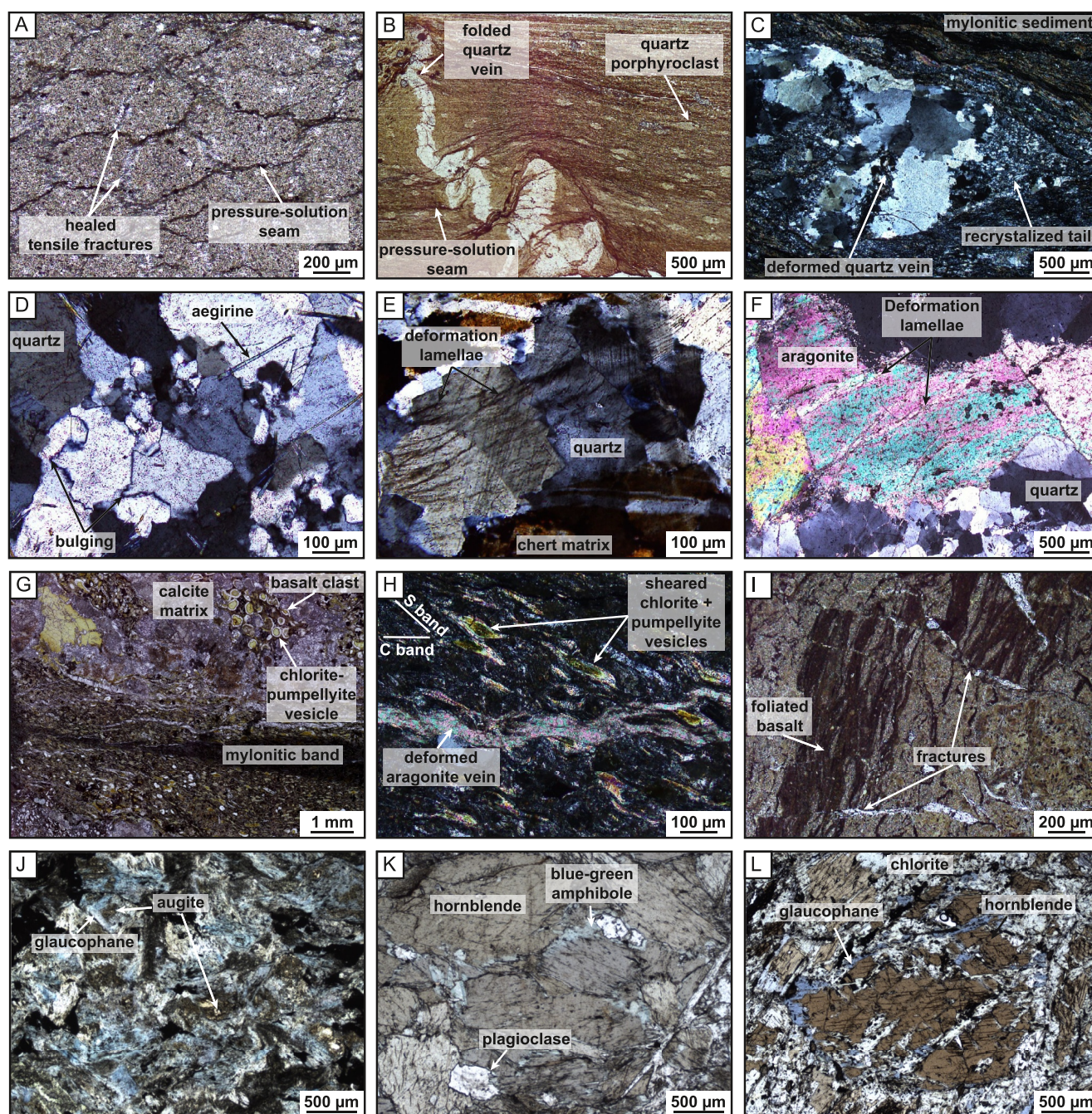


Figure 5. Petrography of the Snow Mountain Volcanic Complex and surroundings (2/2). (a) Deformed fine-grained Upper graywacke sample with pressure-solution seams and quartz-carbonate-filled tensile fractures (SM19-18; Snow Mountain summit area below the West Summit thrust; Figure 3c). (b) Mylonitic clastic sediments with folded quartz veins and flattened quartz porphyroclasts (SM20-62; top thrust). (c) Boudinaged quartz vein in mylonitic sediment with recrystallized tails (SM20-63; top thrust). (d) Portion of an aegirine-quartz vein in a chert, showing bulging of quartz along grain boundaries (SM19-19; Snow Mountain summit area below the West Summit thrust; Figure 3c). (e) Textures of quartz internal deformation in the same vein, showing undulose extinction and thin and thick deformation lamellae. (f) Deformation lamellae in vein aragonite in basalt (SM19-23; Snow Mountain East Summit). (g) Mylonitic band and strong strain gradients in basalt marked by flattened chlorite-pumpellyite-bearing vesicles, later affected by brecciation and calcite infiltration (SM20-13; West summit thrust). (h) Zoom on the mylonitic band of the same sample, showing flattened and sheared pumpellyite-chlorite porphyroclasts (former vesicles) and a deformed aragonite vein. (i) Superimposed ductile (foliation) and brittle (fractures) deformation in basalt (SM20-55; top thrust). (j) Microphotograph of a metabasalt with relict augite surrounded by a glaucophane-bearing blueschist-facies assemblage (SM20-03; Middle Fork Stony Creek). (k) Microphotograph of another high-grade block with hornblende with blue-green amphibole retrogression (SM20-46; between the Snow Mountain and Saint John Mountain massifs). (l) Microphotograph of high-grade block SM20-67 (North Fork Stony Creek) showing hornblende surrounded by glaucophane and chlorite.

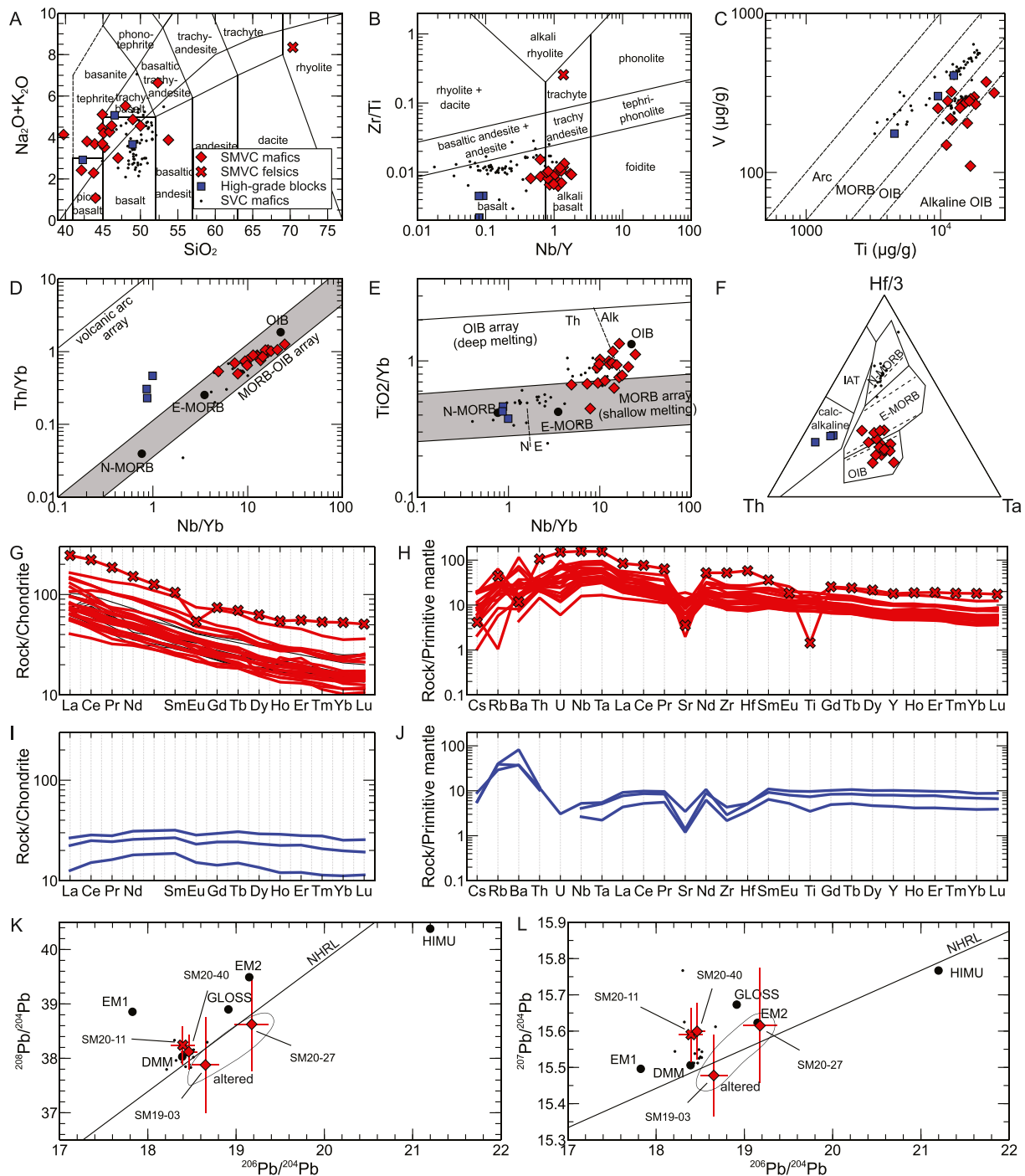


Figure 6. Geochemistry of SMVC volcanic rocks, Stonyford Volcanic Complex (SVC, after Shervais, Zoglman Schuman, & Hanan, 2005) and high-grade blocks. (a) TAS classification (Le Bas et al., 1986). The central line is the sub-alkaline-alkaline limit after Kuno (1968). (b) Classification based on immobile elements, after Pearce (1996). (c) V-Ti discrimination diagram after Shervais (2022). (d) Th/Yb-Nb/Yb discrimination diagram after Pearce (2008). (e) TiO₂/Yb-Nb/Yb discrimination diagram after Pearce (2008). (f) Th-Hf-Ta diagram after Wood (1980). (g) Chondrite-normalized rare-earth element diagram and (h) primitive-mantle-normalized spider diagram for mafic and felsic rocks from the SMVC. Black lines on (f) are analyses from the Stonyford Volcanic complex (Shervais, Zoglman Schuman, & Hanan, 2005). (i) and (j) Similar diagrams for mafic high-grade rocks. (k and l) Pb isotope of samples (age-corrected at 167 Ma), and mantle source end-member isotopic compositions. Error bars are $\pm 2SE$ of the replicates. DMM: Depleted MORB Mantle, EM1: enriched mantle 1, EM2: enriched mantle 2, HIMU: high μ ($=^{238}U/^{204}Pb$; values after Jackson & Dasgupta, 2008), GLOSS: global subducted sediment (Plank & Langmuir, 1998), NHRL: northern hemisphere regression line (Hart, 1984). Trace element concentrations are normalized to the chondrite and primitive mantle values of McDonough and Sun (1995) and Sun and McDonough (1989).

5.2. Snow Mountain Felsic Rock

The felsic rock from the Snow Mountain Volcanic complex plots as a rhyolite in the TAS diagram (Figure 6a), and as a trachyte in the Zr/Ti – Nb/Y diagram (Figure 6b). It is not plotted in other discrimination diagrams which are only suited for mafic rocks. Chondrite-normalized REE diagrams show higher REE concentrations than in the mafic rocks with the same decreasing trend (La and Lu concentrations 251 times and 50 larger than chondrite, respectively), and a notable Eu negative anomaly (Figure 6g). The extended spider diagram additionally shows a negative Ti anomaly (Figure 6h). With LILE concentrations similar to SM20-40, SM20-11 has very similar $^{206}\text{Pb}/^{204}\text{Pb}_{167\text{ Ma}}$, $^{207}\text{Pb}/^{204}\text{Pb}_{167\text{ Ma}}$ and $^{208}\text{Pb}/^{204}\text{Pb}_{167\text{ Ma}}$ of 18.396 ± 0.135 , 15.590 ± 0.074 and 38.242 ± 0.347 , respectively (Figures 6k and 6l), again overlapping with depleted MORB mantle.

5.3. High-Grade Blocks

High-grade blocks around the SMVC have a mafic protolith and plot as picro-basalt, basalt, and trachy-basalt in the TAS diagram (Figure 6a) and in the basaltic field of the Zr/Ti – Nb/Y diagram (Figure 6b). They all plot in the MORB field of the V – Ti diagram (Figure 6c), but they plot in the volcanic arc array of the Th/Yb – Nb/Yb (Figure 6d). They plot in the calc-alkaline field of the Th – Hf – Ta diagram (Figure 6f). Chondrite-normalized REE diagrams are relatively flat, with a slight upward bend for the middle REE, and low overall concentrations in REE (11–32 times higher than chondrite for all REE; Figure 6i). Extended spider diagrams display positive Rb–Ba anomalies, and slightly negative Nb–Ta anomalies, negative Sr and Zr–Hf anomalies for all samples (Figure 6j).

6. Mineral Compositions and Conditions of Metamorphism

Metamorphic rocks were sampled both from the SMVC (low-grade metamorphism) and more pervasively recrystallized high-grade blocks cropping out in the TCSM and between the Snow Mountain and Saint John Mountain massifs (Figure 2a). Mineral compositions in 26 samples were analyzed by electron microprobe, and mapping was performed on one sample. Pressure-temperature conditions were determined through Raman Spectroscopy on Carbonaceous Material (RSCM; Lahfid et al., 2010) for 11 samples, multi-equilibrium thermobarometry for one sample and pseudosection modeling was performed for two metamorphic parageneses of one sample. Detailed procedures are available in Text S3 of Supporting Information S1.

6.1. The Snow Mountain Complex: Incipient Blueschist Facies

Despite limited recrystallization of SMVC magmatic rocks, metamorphic index minerals were recovered throughout the complex, in particular lawsonite, aragonite, blue amphibole and clinopyroxene (Figure 2a). Metamorphic clinopyroxene in veins is aegirine, usually with a strong zoning between jadeite and aegirine endmembers, with a maximum jadeite content of 48% (Figures 7a–7c). Lawsonite throughout the SMVC has a range of compositions, along the Fe,Ti = Al substitution in octahedral sites (Figure 7d).

RSCM thermometry was carried out on two samples from the SMVC *Upper Graywacke* and one sample potentially belonging to the *Summit Spring Sequence* a few meters below mafic volcanics of Snow Mountain Massif (Figures 2a and 2b). Thermometry yields maximum values of $236 \pm 7^\circ\text{C}$, $242 \pm 8^\circ\text{C}$, and $246 \pm 9^\circ\text{C}$ respectively (2SE internal uncertainty, Figure 8a).

Moreover, the presence of key high pressure–low temperature index minerals such as lawsonite, blue amphibole, sodic clinopyroxene and aragonite are key to defining pressure. In particular, the abundance of lawsonite + quartz within veins (Figures 4j and 4k) suggests pressures above 0.2 GPa, and the widespread occurrence of aragonite veins (Figures 4i, 5f, 5h) indicates that metamorphism occurred at pressure above 0.5 GPa (given a temperature of 240°C , Figure 8b).

Independent estimates of pressures are obtained from the albite-aegirine-quartz vein assemblage, using the univariant reaction albite = jadeite + quartz. The highest jadeite content in clinopyroxene (48%) is compatible with a peak pressure of ~ 0.6 GPa at 240°C using the Average Pressure mode of Thermocalc (Figure 8b).

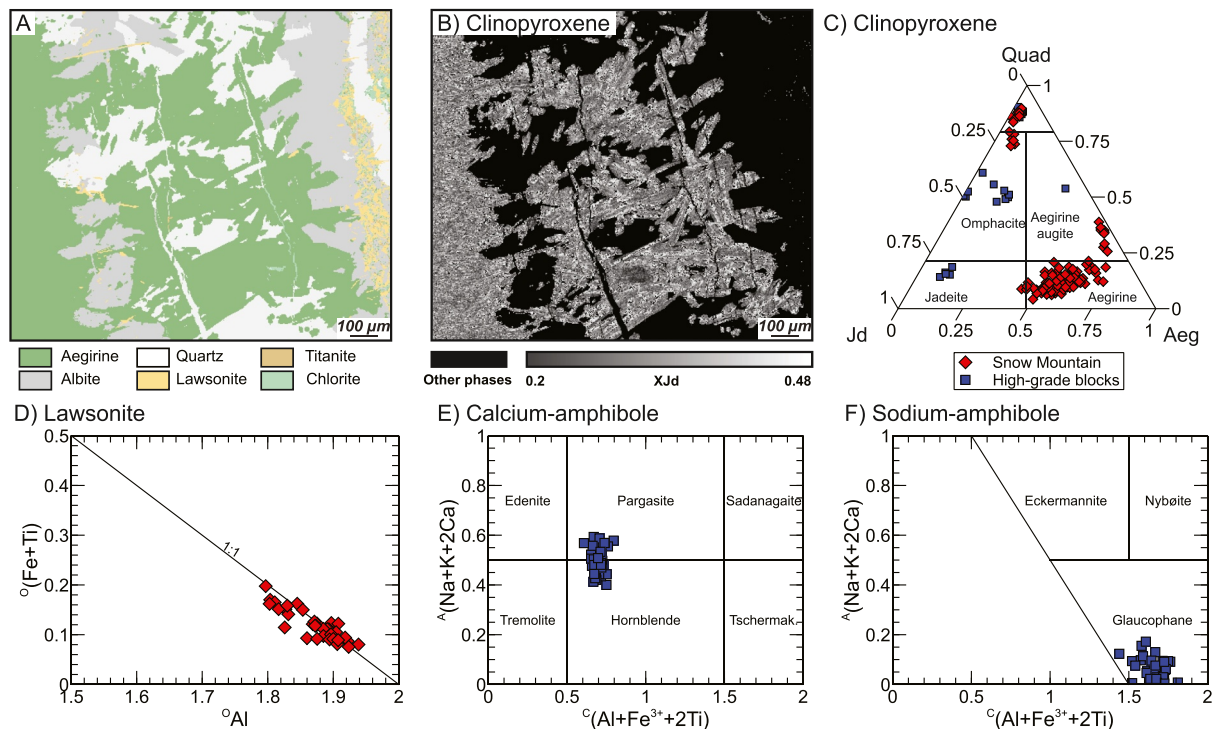


Figure 7. Mineral compositions. (a) EPMA phase map showing the composition of a metamorphic vein in the SMVC (SM19-27; Figures 4j and 4k). (b) Detailed composition of clinopyroxene in the same vein. (c) Composition of magmatic (Quad) and metamorphic clinopyroxene crystals in the SMVC and high-grade blocks. (d) Spread of lawsonite composition in the SMVC along the $\text{Al} = \text{Fe} + \text{Ti}$ substitution line. (e) Composition of calcium-amphibole in high-grade block SM20-67 from the TCSM. (f) Composition of sodium-amphibole in high-grade block SM20-67 from the TCSM.

6.2. Sedimentary Rocks-Dominated Franciscan Units

Sedimentary rocks sampled from fault zones structurally below, within and above the SMVC (some areas mapped as *Summit Spring Sequence* or Franciscan complex by MacPherson (1983)) were screened for carbonaceous matter. Thermometry by RSCM yields clustered temperatures depending on the structural position (Figure 8a): 222–225°C for three samples below the SMVC, 236–246°C for three samples within the Snow Mountain massif of the SMVC, 247–259°C for three samples above the Saint John Mountain massif of the SMVC, and 279–309°C for four sediment samples between the Snow Mountain and Saint John Mountain massifs (associated with serpentinite and high-grade blocks from the TCSM, hence interpreted as belonging to tectonic slivers above the SMVC).

6.3. High-Grade Rocks: Amphibolite to Upper Blueschist Facies

The three high-grade rocks have different metamorphic histories. In samples SM20-03 and SM20-45-2, the occurrence of omphacite/jadeite (Figure 7c) and glaucophane (Figure 7f) indicates metamorphism at upper blueschist-facies conditions. Such assemblages are shown to exist around 300–450°C and 0.7–1.5 GPa in rocks of similar protolith (Diener & Powell, 2012; Plunder et al., 2015). By contrast, sample SM20-67 was affected by two episodes of metamorphism, marked by two amphibole generations (Figure 5l): first at high temperatures with hornblende-pargasite (Figure 7e; Si between 6.15 and 6.20 apfu; Ti between 0.18 and 0.20 apfu) + titanite (Zr between 200 and 300 $\mu\text{g.g}^{-1}$), then at blueschist-facies conditions with glaucophane (Figure 7e; $^{\text{B}}\text{Na}$ above 1.92 apfu), omphacite (Figure 7c; $\text{XMg} = \text{Mg}/(\text{Mg} + \text{Fe}^{2+})$ between 0.57 and 0.59), white mica (Si between 3.4 and 3.5 apfu) and chlorite (XMg between 0.58 and 0.60). P - T - O_2 pseudosection modeling combined with conventional thermobarometry best reproduce the observed mineral assemblages and compositions around 785–810°C and 0.9–1.1 GPa for the first stage at high-temperature conditions (Figure 8c; Figure S4 in Supporting Information S1), and around 400–425°C and 1.5–1.8 GPa for the second stage at upper blueschist-facies conditions (Figure 8d; Figure S4 in Supporting Information S1).

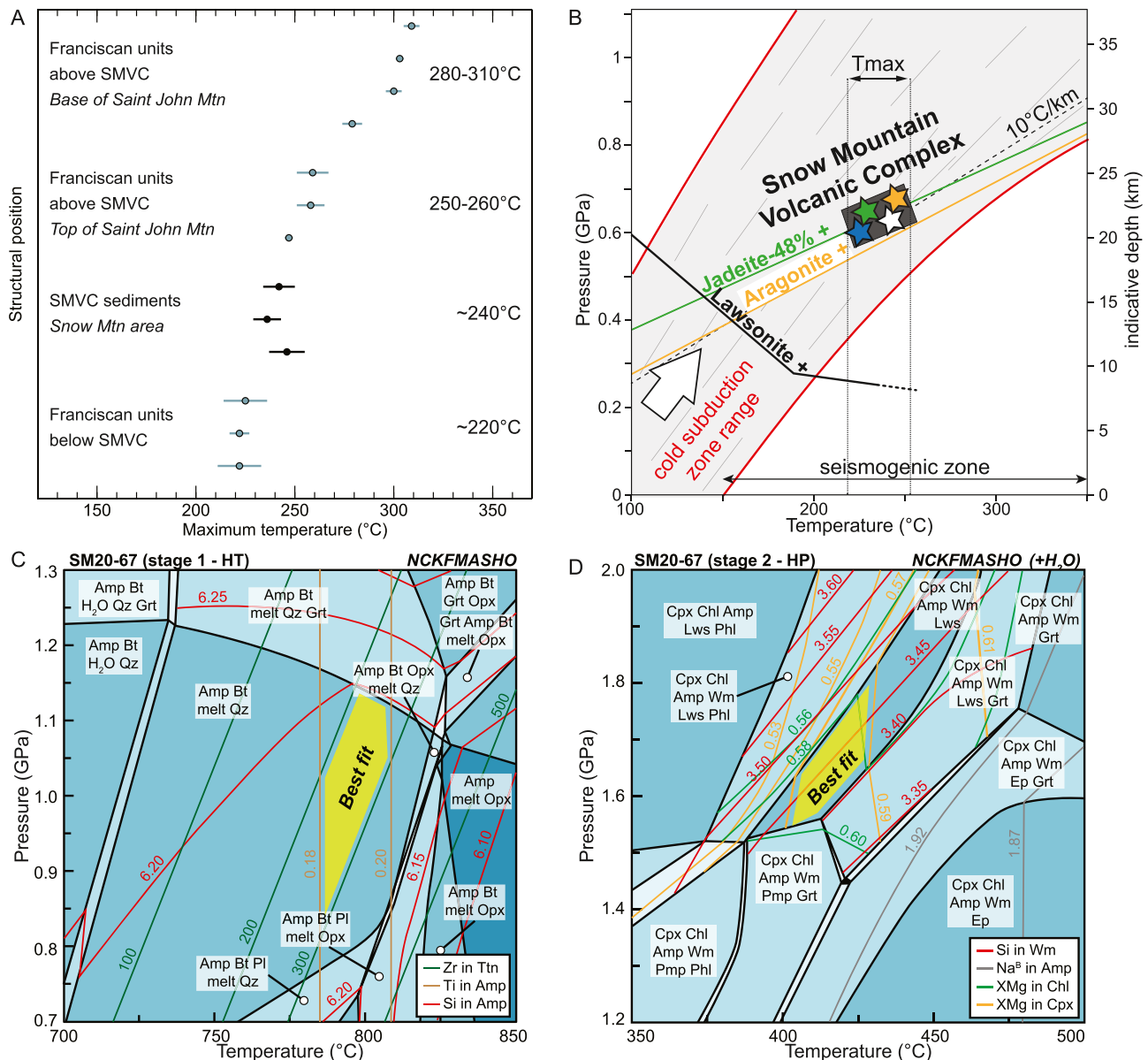


Figure 8. Conditions of metamorphism. (a) Synthesis of RSCM data for the SMVC and Franciscan units above/below. Uncertainty shown is the internal 2SE and weighted mean is calculated for all subsets. (b) P - T conditions for the SMVC, based on RSCM thermometry, carbonate polymorph and albite-jadeite-quartz equilibrium. (c) Phase equilibrium modeling of the high-temperature (HT) stage of sample SM20-67. Titanium isopleths in amphibole are derived from the thermometer of Liao et al. (2021). Zirconium isopleths in titanite are calculated from the thermobarometer of Hayden et al. (2008). (d) Phase equilibrium modeling of the high-pressure (HP) stage of SM20-67 at blueschist-facies. Mineral abbreviations: Amp, amphibole; Bt, biotite; Chl, chlorite; Cpx, clinopyroxene; Grt, garnet; Lws, lawsonite; Opx, orthopyroxene; Phl, phlogopite; Pmp, pumpellyite; Qz, quartz; Wm, white mica. XMg = Mg/(Mg + Fe²⁺), with Mg and Fe²⁺ expressed in atoms per formula unit (apfu).

7. Accessory Mineral U-Pb Geochronology and Trace-Element Geochemistry

Simultaneous U-Pb geochronology and simultaneous trace-element analyses were carried out by laser ablation split-stream ICP-MS at the University of California, Santa Barbara. Zircon was analyzed in one magmatic sample and in three detrital samples and titanite was analyzed in situ in one sample. Details of the procedures are available in Text S3 of Supporting Information S1, location of the titanite analyses in Figure S5 of Supporting Information S1, and cathodoluminescence images of the zircons in Figure S6 of Supporting Information S1.

7.1. Magmatic Zircon Geochronology

Zircons within the rhyolite sample (SM20-11) from the *West Summit Sequence* yield concordant U-Pb dates with Th/U ratios of 0.3–0.9. Thirty-nine dates (out of 40) produce a weighted mean $^{238}\text{U}/^{206}\text{Pb}$ date of 166.1 ± 0.6 Ma (MSWD = 1.1). All analyses display REE patterns with positive Ce anomalies, negative Eu anomalies, and positive heavy REE slopes.

7.2. Titanite Geochronology

Two populations of titanite are identified in high-grade sample SM20-67 by their REE patterns, one with negative slope of heavy REE concentrations relative to chondrite, and one with flat HREE profiles and a positive Eu anomaly (Figure 9d). Because these two populations are undistinguishable in age and textural context, they were grouped for age calculation and produce a discordia date of 170.5 ± 1.6 Ma ($n = 54/54$; MSWD of 1.9, using the algorithm of York (1967)).

7.3. Detrital Zircon Geochronology

Zircon from sample SM20-38 produces dates between 145.8 ± 3.4 and $2,445 \pm 14$ Ma ($n = 172$; Figure 9e). Age peaks including more than 10 zircon grains occur at ~ 200 Ma, ~ 160 Ma, and ~ 150 Ma. The maximum depositional age is estimated to be 148.5 ± 0.6 Ma from a statistically homogenous population of 25 zircons.

Zircon from sample SM19-18 yields dates between 116.3 ± 2.0 Ma and $2,795 \pm 70$ Ma ($n = 189$; Figure 9e). Age peaks including more than 10 zircon grains occur at ~ 160 and ~ 150 Ma. The maximum depositional age is estimated to 118.4 ± 0.7 Ma based on a statistically homogenous population of six zircons.

Zircon from sample FASM18-03 produces dates between 98.3 ± 1.7 Ma and 1871.5 ± 77.2 Ma ($n = 197$; Figure 9e). Age peaks including more than 10 occur at ~ 169 Ma, ~ 160 Ma, ~ 148 Ma and 101 Ma. The maximum depositional age is estimated to be 100.6 ± 0.2 Ma from a statistically homogenous population of 63 zircons.

8. Discussion

8.1. The Snow Mountain Volcanic Complex: A Seamount on the Farallon Plate

The geology of the Snow Mountain Volcanic Complex has extensively been described by MacPherson (1983). Here, we review and discuss the robustness of his main arguments in light of our own findings.

8.1.1. Geological Evidence for a Seamount Origin

The SMVC formed as a submarine volcano, as attested by the large volumes of (mainly pillowed) volcanic rocks, pillow breccia, and local radiolarian chert cover. The overall size of the complex is around 12×20 km, with a minimum thickness of ~ 600 m. The largest continuous portion is larger than 7×16 km, which makes the SMVC as one of the largest on-land portions of oceanic lithosphere (e.g., the Oman and Newfoundland ophiolites with continuity along >100 km, Belgrano et al., 2019; Dewey & Bird, 1971; Nicolas, 2000) and former subducted seamounts (Anarak seamount, Bagheri & Stampfli, 2008; Siah Kuh seamount, Bonnet et al., 2020, Bonnet, Agard, Angiboust, Fournier, & Omrani, 2019, Bonnet, Agard, Angiboust, Monié, et al., 2019). Eruption of the SMVC on top of the deep-sea sediments of the *Summit Spring Sequence* (intrusive relationship shown on Figure 4 of MacPherson (1983)) requires a preexisting oceanic lithosphere, as expected for a seamount (e.g., Staudigel & Clague, 2010).

The upward-increasing vesicularity of the mafic volcanics observed by MacPherson (1983) and in this study may record shallowing eruption depth (above 2 km; e.g., Moore, 1965). MacPherson (1983) described ropy lava textures in the uppermost portions of Snow Mountain (not observed in our study) and suggested that these could have been derived from atmospheric eruptions. However, such ropy textures could also form underwater (e.g., Embley & Rubin, 2018).

Contrary to other exhumed subducted seamounts, the SMVC does not have a carbonate cap that could be representative of a former carbonate platform formed at shallow depth. Instead, radiolarian chert within the SMVC (*Upper Chert* of MacPherson (1983)) was most likely deposited below the carbonate compensation depth, which oscillated between 3 and 4 km depth from the Late Jurassic to Late Cretaceous (Van Andel, 1975), although

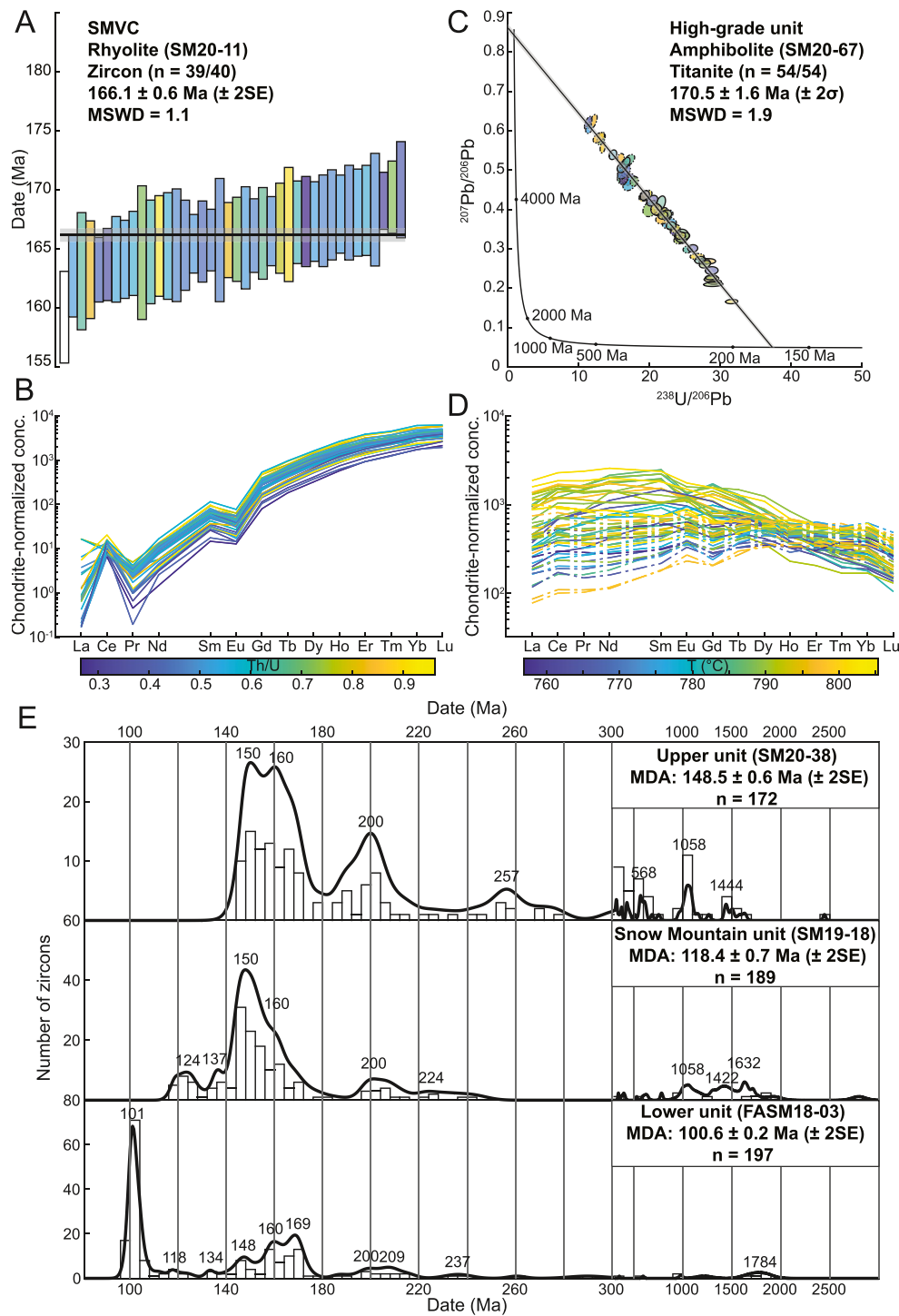


Figure 9. U-Pb geochronology of the SMVC and surrounding units. (a) Zircon geochronology (weighted mean $^{238}\text{U}/^{206}\text{Pb}$ date) of a rhyolite from the SMVC. Color scale is the same as in (b). (b) Chondrite-normalized Rare-earth element (REE) patterns of the dated zircons. Color scale is the Th/U ratio. Reference values for chondrite normalization are from McDonough and Sun (1995). (c) Titanite geochronology of high-grade block SM20-67 (Tera-Wasserburg diagram). All ellipses were used in age calculation. Colorscale is the same as in (d). (d) Chondrite-normalized REE patterns of the dated titanite. Dotted patterns are the same as in C, and have a distinct chemistry. The color scale is the Zr-in-titanite temperature, estimated at 1 GPa. (e) Detrital zircon geochronology results for three samples, shown as probability density curves and 5 My-box histograms. Dates of the main peaks are shown above the curve. MDA is the maximum depositional age.

this is strongly impacted by local carbonate productivity. Therefore, there is no definitive evidence of shallow water/subaerial eruption.

The occurrence of siliciclastic sediments (mainly graywacke) on top of the SMVC (as part of the *Upper Graywacke*) and in the *Summit Spring Sequence* (as mapped by MacPherson (1983)) may appear counterintuitive for the interpretation of the SMVC as a seamount. Such deposits are not characteristic of deep ocean, low-energy depositional environments, but rather of trench environments, where incoming oceanic material may be covered by detrital input from the accretionary wedge and arc. This explanation is consistent with the structural position of the *Upper Graywacke* unit, that is discordant at the top of the SMVC (Figure 3c) and likely reflects the last stage of oceanic sedimentation, possibly long after the eruption of the SMVC. However, in the area mapped as the *Summit Spring Sequence* (Figure 2a) assumed to be constituted of pre-eruptive sediments (MacPherson, 1983), graywacke is volumetrically dominant. These occurrences of graywacke are most likely late tectonic intercalations that do not belong to pre-SMVC sediments. This is shown by (a) their occurrence along fault zones (below Snow Mountain and between Snow Mountain and Saint John Mountain), (b) their association with allochthonous serpentinite, (c) maximum metamorphic temperatures significantly different than those of Snow Mountain's *Upper Graywacke*, and (d) maximum depositional ages from detrital zircons much younger than the volcanism in the SMVC (Figure 9e). Additionally, our study shows that some radiolarian cherts within the mapped *Summit Spring Sequence* are significantly younger (upper Kimmeridgian-lower Tithonian to Valanginian, i.e. ~155–130 Ma) than the eruption of the SMVC (~166.5 Ma), which indicates that even some of the deep-sea sediments are not pre-eruption sediments. We therefore suggest that a significant part of what has been mapped as the *Summit Spring Sequence* corresponds to Franciscan units imbricated below and within the SMVC, either during subduction, or during later tectonic activity, and has no genetic link with the SMVC.

In summary, a seamount origin is strongly supported by the size and eruption on top of sediments of the SMVC, at least locally. Yet, geological arguments for a shallow eruption are disputable. A more precise assessment of its origin requires additional geochemical screening.

8.1.2. Geochemical Evidence for a Seamount Origin

Bulk rock analyses performed in this study (Figure 6) yield comparable results to mineral and bulk-rock analyses by MacPherson (1983) and Shervais and Kimbrough (1987). Major element analyses show that mafic volcanics are distributed along an alkaline trend from picro-basalt to basaltic trachy-andesite. Trace elements confirm the alkaline trend from mafic to felsic rocks, with elevated normalized LREE to HREE ratios. Snow Mountain rocks are classified along a mixing trend between E-MORB and OIB. Pb isotope measurements in the least-altered samples indicate a depleted MORB mantle source comparable to the Hawaii and Galapagos sources (Jackson & Dasgupta, 2008). Such signatures were modeled in alkali basalts from the Stonyford Volcanic Complex to derive from 10% to 15% non-modal partial melting of an E-MORB-type spinel-lherzolite (Shervais, Zoglman Schuman, & Hanan, 2005). Melting of a more-enriched source (intermediate between E-MORB and OIB, as suggested for the SMVC and the Stonyford Volcanic Complex) would give similar trace element patterns at lower fusion rates. Such a pattern is representative of off-ridge volcanism, as along modern hotspot tracks (e.g., Piton de la Fournaise volcano above the Réunion hotspot, Albarède & Tamagnan, 1988). Integration of these geochemical results is therefore consistent with an origin of the Snow Mountain Volcanic Complex as a within-plate volcano erupted atop older oceanic crust.

Alkaline basaltic rocks from the nearby Stonyford Volcanic Complex, alternatively interpreted as part of the Coast Range Ophiolite (Arkula et al., 2023; Choi et al., 2008; Shervais & Kimbrough, 1985a; Shervais, Zoglman Schuman, & Hanan, 2005) or Franciscan Complex (Hopson & Pessagno, 2005; MacPherson & Phipps, 1985) share striking similarities in both age and alkaline chemistry with the SMVC. Such similarities were highlighted by MacPherson and Phipps (1985), and are confirmed by our precise dating of the SMVC. However, four main distinctions can be made between the SMVC and the Stonyford Volcanic Complex: (a) the significant chemical variability in the Stonyford Volcanic Complex (including alkali basalts, but also oceanic tholeiites and high-aluminum and low-titanium basalts) is not observed in the SMVC; (b) the difference in the stratigraphy of both units; (c) the absence of younger than Jurassic rocks (including clastic sedimentary rocks) on top of the Stonyford Volcanic Complex; and (d) the absence of high-pressure mineral assemblages in the Stonyford

Volcanic Complex. We hence propose that the similarities between the SMVC and the Stonyford Volcanic Complex are merely coincidental.

8.2. Subduction of the Snow Mountain Volcanic Complex in the Seismogenic Zone

8.2.1. Incipient Blueschist-Facies Metamorphism Triggered by Local Fluid-Rock Interactions

The metamorphic imprint of the Snow Mountain Volcanic Complex is limited to a few metamorphic minerals replacing primary magmatic assemblages but is most significant in vein assemblages. Peak pressure-temperature conditions estimated from those veins are around 240°C and 0.6 GPa (or ~20 km burial assuming lithostatic pressure and a 3,000 kg/m³ density for overlying—mainly mantle—rocks; Figure 10a). These conditions correspond to a high-pressure and low-temperature metamorphic gradient of ~10°C/km typical of subduction zones (Agard et al., 2018). This estimate confirms and refines that of MacPherson (1981) at 200–325°C and 0.6–1.0 GPa for the surrounding units. The preservation of metamorphic aragonite and lawsonite requires limited reaction and perhaps minimal heating during fast exhumation (Gillet & Goffé, 1988). The peak metamorphic temperature and density of high-pressure mineral-bearing veins increase at the NE part of the SMVC, consistently with the Mesozoic subduction direction of the Farallon Plate (Figure 2a; Ring & Brandon, 1994), as those areas likely represent the deepest/warmest subducted portions of the unit (favoring metamorphic reactions).

Questions arise whether estimated metamorphic conditions indeed represent peak metamorphism. Metamorphic minerals formed preferentially in veins, whereas rock matrices remained almost unaffected by metamorphic transformations due to very slow kinetics at low temperature, that is, thermodynamically-predicted reactions are significantly overstepped (Pattison et al., 2011). Some kinetic effects cannot be completely excluded in veins, as shown by zoning in clinopyroxene (Figures 7b and 7c; e.g., Watson & Liang, 1995) that possibly affect average pressure calculations. However, the occurrence of aragonite in veins is a good indicator for a minimum pressure of 0.6 GPa (Figure 8b), while kinetics of carbonaceous matter transformation are fast enough for RSCM temperatures to indeed be representative of maximum temperatures (Nakamura et al., 2017).

The potential of subducting seamounts to be subject to tectonic overpressure (deviatoric pressure, as modeled by Ruh et al. (2017)) has been discussed in Bonnet, Agard, Angiboust, Monié, et al. (2019). Internal deformation of the seamount (see following paragraph) makes large overpressure unlikely. However, fluid pressure in veins within rocks affected by deviatoric stress may exceed lithostatic pressure (e.g., Hosokawa & Hashimoto, 2022; Sibson, 2004). The occurrence of similar high-pressure assemblages in veins, irrespective of vein orientation (e.g., Figure 4j) suggests that fluid pressure is not much higher than lithostatic pressure. Moreover, mineral precipitation from the fluid must occur when the pressure (i.e., solubility) diminishes, due to drainage of the fluid (Sibson, 2004). In this case, index minerals in veins would rather imply minimum pressures.

8.2.2. Long-Term Deformation: Local and Transient Strain Localization in the Snow Mountain Seamount

The deformation structures in the SMVC are at first sight comparable to those observed in other subducted seamount: deformation was accommodated above, within and below the seamount (Figure 3a). Deformation above the seamount is expected during subduction of the seamount, and is visible in the top thrust above the SMVC (interface 1, Figures 10b and 11b). While deformation might be localized along a thin plate interface when a smooth ocean plate subducts (e.g., Agard et al., 2018; Bebout & Penniston-Dorland, 2016), seamount subduction is likely associated to transient thickening of the subduction interface (Lallemand et al., 1994; Munoz-Montecinos et al., 2023; Noda et al., 2020) together with diffuse deformation of the upper plate (Dominguez et al., 1998; Ranero & von Huene, 2000; Wang & Bilek, 2011). The mylonitic sedimentary sliver located above Snow Mountain on Saint John Mountain eastern slopes (Figures 5b and 5c), with *P-T* conditions in agreement with that of the SMVC (Figure 8a), hints to such upper plate deformation, as it possibly corresponds to a formerly accreted unit that was tectonically eroded and bulldozed down during subduction of the SMVC.

Upon reaching peak metamorphism (i.e., 240°C and 0.6 GPa), deformation must have progressively localized within and below the seamount to allow any underplating and exhumation (Figures 10b and 11b), as shown by Bonnet, Agard, Angiboust, Monié, et al. (2019). Deformation within the SMVC is clearly visible along internal thrusts (Figure 3a), some of which cut through the entire complex and were therefore the surfaces on which the seamount was partially decapitated at depth (as proposed for Chilean, accretionary-type margins by Cloos &

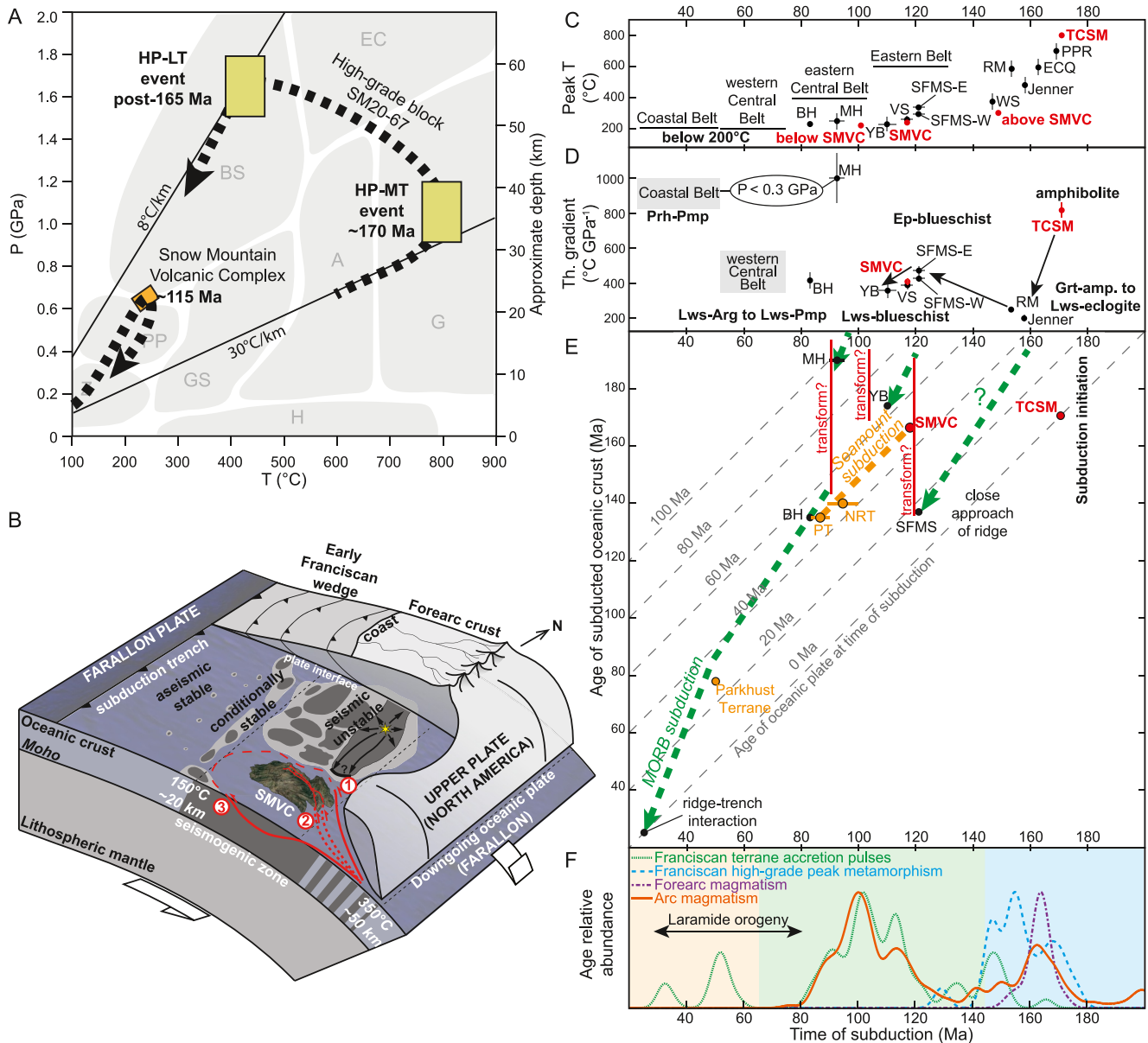


Figure 10. Synthesis of the results and interpretations of this study. (a) Synthesis of P - T conditions and P - T paths of the Snow Mountain seamount and of one intercalated high-grade block of the TCSM (SM20-67), and corresponding ages. Note that P - T paths may be more complex than schematically shown. Facies abbreviations: A, amphibolite; BS, blueschist; EC, eclogite; G, granulite; GS, greenschist; H, hornfels; PP, prehnite-pumpellyite; Z, zeolite. (b) 3D sketch of the SMVC at peak burial, and potential implications for seismogenesis (adapted from Bonnet, Agard, Angiboust, Fournier, & Omrani, 2019; Bonnet, Agard, Angiboust, Monié, et al., 2019). 1, 2, and 3 refer to transient subduction interfaces. (c) Regional evolution of peak metamorphic temperatures against approximate subduction/peak metamorphic age showing overall decrease of maximum temperatures with time. Data include high-grade blocks (Anczkiewicz et al., 2004; Ravna & Terry, 2004; Tsujimori et al., 2006), Eastern Belt units (Dumitru et al., 2010), Central and Coastal Belt units (Dumitru et al., 2015; Ernst & McLaughlin, 2012; Meneghini & Moore, 2007; Tagami & Dumitru, 1996; Terabayashi & Maruyama, 1998). Abbreviations of subducted terranes: BH, Burnt Hills Terrane; ECQ, El Cerrito Quarry; MH, Marin Headlands; NRT, Nicasio Reservoir Terrane; PPR, Panoche Pass Road; PT, Permanente Terrane; RM, Ring Mountain; SFMS-E/W: South Fork Mountain Schist (east and west); VS, Valentine Spring; WS, Willow Springs; YB, Yolla Bolly. (d) Regional evolution of the metamorphic thermal gradient recorded in Franciscan units, showing fast cooling of high-grade blocks (in less than ~ 10 My), followed by a second main accretion period with long-term decrease of the thermal gradient. Same data sources as (c). Bold black text corresponds to the usual metamorphic facies. Abbreviations refer to: Arg, aragonite; Ep, epidote; Grt-amp., garnet amphibolite; Lws, lawsonite; Pmp, pumpellyite; Prh, prehnite; (e) Subduction versus eruption age for the crust comprised in the main accreted Franciscan units, modified after Murchey and Blake (1993), Wakabayashi (2015, 2017b). Crust age at subduction is marked by diagonal dashed gray lines. Off-axis seamount volcanism must be younger (i.e., below in this graph) than underlying MORB crust. Sharp changes of MORB crust age at subduction may be linked to the subduction of transform faults (hypothetical location marked by solid red lines). (f) Probability density curve of subduction ages of Franciscan units, showing the main accretionary pulses (Apen et al., 2021, and references therein), peak high-grade metamorphism (data from zircon U-Pb, and garnet and lawsonite Lu-Hf; and titanite U-Pb from this study; and synthesis by Mulcahy et al. (2018)), Coast Range Ophiolite forearc magmatism (data from zircon, apatite and titanite U-Pb and glass Ar-Ar; Mulcahy et al., 2018, and references therein), and Sierra Nevada magmatic arc plutons (Barth & Wooden, 2006; Barth et al., 2008; Needy et al., 2009).

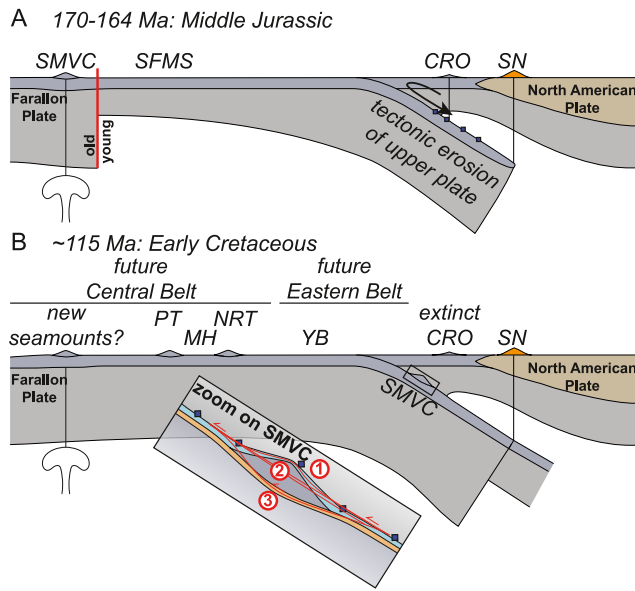


Figure 11. Simple evolution sketch for the Franciscan subduction zone. (a) Middle Jurassic setup: eruption of the SMVC on top of the Farallon plate, while subduction is ongoing at the North American margin, favoring forearc magmatism, arc magmatism and tectonic erosion (and high-grade metamorphism) of portions of the forearc. The abrupt variation in age of the oceanic lithosphere is accommodated by a large-offset transform fault. (b) Early Cretaceous setup with the SMVC at peak metamorphism. New seamounts are potentially erupted at this time on the Farallon plate. Numbers on zoom inset refer to successive plate interfaces. Abbreviations: CRO, Coast Range Ophiolite; MH, Marin Headlands; NRT, Nicasio Reservoir Terrane; PT, Permanente Terrane; SFMS, South Fork Mountain Schist; SN, Sierra Nevada; YB, Yolla Bolly.

Shreve, 1996). This internal deformation is observable in two areas. The first area is the *West Summit thrust*, where basaltic rocks from the hanging wall are deformed across ~20 m and progressively developed a cleavage, and the thrust is rooted in trench-derived sediments of the *Upper Graywacke*. The second area is the *intermediate thrust zone*, where multiple faults cut across the SMVC, separating the Snow Mountain and Saint John Mountain massifs, and caused the intercalation of other Franciscan units (likely from the upper plate). The convex horseshoe shape (Figure 2a) of these decameter-to-hectometer-thick fault zones is reminiscent of that observed in the Siah Kuh unit (Bonnet, Agard, Angiboust, Monié, et al., 2019). Displacements along these faults (interface 2; Figures 10b and 11b) are likely of the order of one to a few kilometers because no major changes in lithology of the SMVC are observed across them. Deformation along these faults predominantly occurred near the peak metamorphic phase. This is evidenced by (a) deformed high-pressure assemblages (yet without aragonite replacement by calcite, as would be expected if deformation took place at lower pressure conditions), (b) compatibility of structures with inferred subduction direction (Ring & Brandon, 1994) and (c) the increase in metamorphic vein density around them. Although these faults must have been originally nucleated within basalt, the intercalation of rheologically weak, water-and-phylosilicate-rich sediments and serpentinite likely favored displacement along these faults (Niemeijer & Spiers, 2005), as shown in Bonnet, Agard, Angiboust, Monié, et al. (2019) and Barbero et al. (2023). The local occurrence of calcite-bearing breccias postdating the high-pressure (aragonite-bearing) deformation suggests that some of these faults were reactivated after peak metamorphism.

The rocks of the *top*, *intermediate* and *West Summit thrusts* evidence both brittle (vein opening, and small-scale fractures) and ductile (pressure-solution seams, quartz, aragonite and pumpellyite internal deformation, mylonitic fabrics) deformation mechanisms. This is in line with mixed rheological

behavior as observed in other units subducted at similar depth (Ring & Brandon, 1999; Schmidt & Platt, 2022). Additionally, ductile deformation in hydrated basalt is favored by the abundance of pumpellyite and chlorite, that host deformation through dissolution in former vesicles. This highlights the relevance of dissolution-precipitation creep for strain localization within the subduction seismogenic zone.

Deformation at or near the base (interface 3; Figures 10b and 11b) of the seamount is essential to allow the final slicing of the seamount from the downgoing plate prior to exhumation (Bonnet, Agard, Angiboust, Fournier, & Omrani, 2019; Bonnet, Agard, Angiboust, Monié, et al., 2019). In the SMVC, this deformation was localized along the basal thrust of the SMVC, and likely rooted in pre-eruption sediments of the *Summit Spring Sequence* (MacPherson, 1983). The existence of this sedimentary layer at the base of off-axis seamounts has been identified as a weak layer where strain is localized, even in modern ocean islands such as Hawaii (as attested by moderate earthquake activity; Got et al., 2008). However, in the basal thrust of the SMVC, only calcite was identified in carbonate veins (Figure 3i), which suggests that some fluid circulation and possibly slip occurred after peak metamorphism.

Subsequent deformation events along thrust faults characterized by low-pressure mineral assemblages (bearing calcite rather than aragonite) indicate post-peak deformation. This deformation allowed the final assemblage of the SMVC with the SVC. This deformation was preferentially localized in preexisting subduction-related thrust zones.

8.2.3. Short-Term Deformation and Deep Fluid Circulation in the Snow Mountain Seamount

The SMVC was subducted down to ~20 km and ~240°C, conditions that correspond to the middle of the subduction seismogenic zone (Hyndman et al., 1997). Short-term tectonic processes are expected to occur at this depth such as regular earthquakes, but also slow earthquakes (Ide et al., 2007). The potential rock record of such events

has been addressed in many other works (e.g., Giuntoli & Viola, 2022; Herviou et al., 2023; Kirkpatrick & Rowe, 2013), but is still a matter of debate, given the variability of rocks along which deformation is localized. No unequivocal evidence of seismic activity such as pseudotachylite was observed within and at the boundaries of the SMVC.

Multistage veining, generally associated with small displacements (Figures 4j, 4k, and 4l), is however a useful record of fluid pulses in rocks from the SMVC. The existence of these veins requires transient high fluid pressures. Vein opening occurs when pore fluid pressure exceeds the yield strength of rocks, probably due to dehydration during prograde metamorphism. Each vein records several events of fluid circulation, as recorded by crack-seal textures, often observed in accretionary wedges (Herviou et al., 2023). As observed in other seamounts (Bonnet, Agard, Angiboust, Monié, et al., 2019), fluid is most likely released locally by dehydration reactions in basalt (and minor sediments contributing to the carbonate content of these veins), as shown by the reproducible mineralogy of the veins and the absence of leaching haloes (Figure 3j). This local and transient fluid release is probably controlled by deformation and slow reaction kinetics of metabasalt, and focused near peak metamorphism in the deepest subducted parts of the Snow Mountain seamount. An interplay between fluid release and strain localization is likely, since the areas with the largest vein densities are also areas where strain is localized in thrust zones. Episodic fluid release from metabasalt might control short-term tectonic events, such as the earthquake cycle (Dal Zilio & Gerya, 2022) or some of the shallowest slow slip events (Condit et al., 2020). The depth, amount, and episodicity of fluid release during subduction must be strongly controlled by mineral metastability. Deeper, externally-produced fluids may however circulate along transient subduction interface and be occasionally trapped in the SMVC, as shown by leaching haloes in the uppermost part of the SMVC at the subduction interface (Figure 3k). Fluid availability likely enhanced internal deformation mechanisms and reciprocally, ultimately leading to slicing of the SMVC from the downgoing plate.

8.2.4. Is Seamount Exhumation More Common Than Assumed?

Only a few subducted seamounts are reported in exhumed units on Earth, despite the vast number of seamounts on the modern ocean floor (>100,000 bathymetrically-defined seamounts higher than 1 km; Wessel et al., 2010). This has been interpreted to be due to the selectivity of the mechanisms allowing the detachment from the subducting slab and the exhumation of subducted seamounts (Agard et al., 2018), leading most seamounts to be lost in the mantle. Yet, heterogeneities and structural inheritance within and at the base of all seamounts can act as décollement layers where slicing from the lower plate can be localized (Bonnet, Agard, Angiboust, Monié, et al., 2019; MacPherson, 1983). Other authors suggested that rheologically strong intrusive cores may effectively anchor the seamounts to the downgoing plate (Watts et al., 2010).

Although no detailed and exhaustive syntheses exist of potential subducted seamount unit in the Franciscan Complex, a handful of other units have been interpreted as former subducted seamounts in the Franciscan Complex (Figure 1). Wakabayashi (2015) reviewed three potential candidates: the Nicasio Reservoir Terrane (North of the Bay area, with OIB chemistry and seamount structure, Ghatak et al., 2012; Schnur & Gilbert, 2012; erupted >140 Ma and subducted <100 Ma and >85 Ma, Blake et al., 1984; Dumitru et al., 2015; Murchey & Jones, 1984), the Permanente Terrane (South of San Francisco, with OIB chemistry and subduction metamorphism, Ghatak et al., 2012; Larue et al., 1989; erupted >129 Ma, subducted <87 Ma and >63 Ma, Sliter, 1984; Sliter & McGann, 1992; Tarduno et al., 1985), and the Parkhurst limestone in the Coastal Belt (close to Cape Mendocino, erupted >78 Ma, subducted ~50 Ma, Dumitru et al., 2013, 2015; although no bulk rock geochemistry exists for this unit). The Van Arsdale terrane (20 km to the East of the SMVC, Berkland, 1978; Mankinen et al., 1991; erupted ~145 Ma, subducted ~70 Ma, Dumitru et al., 2015; Murchey & Blake, 1993) is likely a good addition. Other units may also have a seamount origin, as shown by enriched MORB to alkaline geochemical signatures near Paskenta, Avila Beach and Aliso Canyon (Shervais & Kimbrough, 1987), the Point Bonita unit in the Marin Headlands (Regalla et al., 2018; Shervais, 1989), although less data is available for these units. The Cazadero-Ward Creek metabasite allochthon, formerly identified as a seamount (Maruyama & Liou, 1988, 1989), has since been shown to be similar to other high-grade units, in terms of age and arc geochemical signature (Wakabayashi & Dumitru, 2007; Wakabayashi et al., 2010). Portions of dismembered seamounts have also been identified based on bulk-rock geochemistry as blocks of variable sizes in shaly mélanges such as in San Simeon (Ukar & Cloos, 2015) and in the Poison Rock Mélange (MacPherson et al., 1990). Overall, seamount material represents >1% of the whole Franciscan Complex outcrops (hence a very significant

proportion of the volcanic volume, since trench-fill clastics make up most of the volume of the subduction complex), while seamounts may represent ~8% of the current ocean floor surface (Etnoyer et al., 2010), an estimate of similar magnitude.

The question whether some of the former examples may belong to a unique seamount chain remains unanswered although an interesting trend emerges from the available and robust geochronological data: the subduction age of the SMVC, the Nicasio Reservoir Terrane, the Permanente Terrane and the Parkhurst limestone gets younger as the eruption ages get younger, with a gap of ~50 Myr between eruption and subduction for the three former examples (Figure 10e).

Inversion using GPlates (Müller et al., 2018) based on eruption and subduction time, and restoration to pre-San Andreas position (Arkula et al., 2023; Wakabayashi, 1999) was performed to test whether the Snow Mountain Volcanic Complex, the Nicasio Reservoir Terrane and the Permanente Terrane could have a unique eruption location in the hotspot reference frame but was not successful. This may be due to the large uncertainty on the geometry and kinematics of the mostly subducted Farallon Plate. Some of this complexity is outlined and discussed below.

8.3. Long-Term Evolution of the Franciscan Subduction Complex and Impact of Seamount Subduction

8.3.1. Franciscan Subduction Initiation and Cooling: Toward a Mature State

The exceptional preservation of the nappe-stack in the Snow Mountain area, far from San Andreas fault branches, enables *P-T* estimates along a continuous km-scale cross-section of the former accretionary complex, from the TCSM (including high-grade metamorphic rocks) down to the Franciscan complex.

High-grade metamorphic rocks from the TCSM lying at the roof the subduction complex occupy a structural position akin to metamorphic soles (structurally above the rest of the Franciscan accretionary wedge, and likely below the Coast Range forearc ophiolite, e.g. Oman, Searle & Malpas, 1980; Newfoundland, Dewey & Bird, 1971). Peak *P-T* metamorphic conditions determined for one mafic block at 800°C and 1 GPa are similar to that of other high-temperature metamorphic soles (e.g., the Oman metamorphic sole, Soret et al., 2017), and are among the hottest found in the Franciscan Complex (Wakabayashi, 1990). The occurrence of tonalitic veins in amphibolitic blocks ~25 km to the north in the same structural position within the TCSM (Shervais et al., 2011) is evidence that moderate amounts of melting occurred in these rocks, as is predicted by the pseudosection model (Figure 8c), and as is common in high-grade metamorphic soles (e.g., Guilmette et al., 2018; Rioux et al., 2016). Contrary to the most classical sole outcrops in Oman and Newfoundland, there are two distinctive characteristics for our sample. First, the occurrence as blocks in a non-isofacial “mélange” and not as a coherent lens below an ultramafic unit of similar grade (Prigent et al., 2018; Soret et al., 2017) or as an isofacial block-in-matrix zone (a feature observed in Tibet; Guilmette et al., 2012). Indeed, the TCSM matrix is likely low grade, as shown by the occurrence of abundant unmetamorphosed blocks (Hopson & Pessagno, 2005; Shervais, Zoglman Schuman, & Hanan, 2005). Second, metamorphic soles are generally strongly deformed (e.g., Agard et al., 2020; Soret et al., 2019), whereas our sample appears only lightly deformed. However, this is likely due to the almost monomineralic (hornblende-supported) composition of the rock, lacking easily-deformed plagioclase or quartz. In fact, some blocks shown by Shervais et al., 2011 in the TCSM, and most Franciscan high-grade blocks are strongly foliated (Wakabayashi, 1990). Hence, these rocks are likely derived from a metamorphic sole, dismembered and assembled at low grade into a “mélange,” an origin discussed for many high-grade blocks in the Franciscan and in the Great Valley Group (Wakabayashi, 2015, 2017a, 2017b).

Magmatic rocks with SSZ affinity (expected in ophiolites formed during subduction initiation; Agard et al., 2023; Stern et al., 2012), exposed in the Southern Coast Ranges (McLaughlin et al., 1988) only occur as blocks within the TCSM and have middle Jurassic ages (Shervais, Murchey, et al., 2005). The SSZ affinities of high-grade blocks in the Franciscan (this study; Ghatak et al., 2012; Saha et al., 2005; Wakabayashi et al., 2010) needs however to be explained, as SSZ rocks are initially formed above a subduction zone, then metamorphosed at high-grade in a subduction zone. Two main models have been proposed to explain this (Wakabayashi et al., 2010): (a) two different subduction zones having different polarity, the second being initiated within the ophiolite erupted above the first; (b) one subduction zone, with progressive subduction erosion of the ophiolite bringing some portions to depth. Wakabayashi (2021) advocate for the first model on structural grounds, yet precise dating of the magmatic protolith of high-grade rocks would be key to understanding their origin, but is so far unavailable.

Titanite associated with the high-temperature assemblage yields a U-Pb date of 170.5 ± 1.6 Ma, interpreted as a crystallization age during prograde to peak metamorphism (see Soret et al. (2022), for a discussion of the interpretation of titanite U-Pb dates in metamorphic sole amphibolites). This age is in line with the oldest ages reported for the prograde to peak metamorphism of high-grade rocks in the Franciscan (garnet Lu-Hf and zircon inclusions-in-garnet U-Pb ages between 177 and 146 Ma; Anczkiewicz et al., 2004; Mulcahy et al., 2018). Amphibole in blocks in similar structural position along a ~ 100 km yields Ar-Ar cooling ages of 168–165 Ma (± 2 –4 Ma; Shervais et al., 2011), interpreted as a pulse of high-grade block exhumation throughout the Franciscan Complex (Rutte et al., 2020), whereas magmatism in the Coast Range Ophiolite is dated at 168–161 Ma (Hopson et al., 2008; Orme & Surpless, 2019). This suggests that the metamorphic sole formed at least ~ 2 My before the main forearc ophiolite remnants, as observed in other ophiolite-metamorphic sole examples (e.g., Oman; Guilmette et al., 2018; Soret et al., 2022; although Rioux et al. (2023) propose that they are contemporary; Turkey, Pourteau et al., 2019). The oldest portions of the ophiolite may however not be preserved (potentially affected by subduction erosion) or may be difficult to date. Finally, the locus of subduction initiation (mid-ocean ridge, transform fault, continental margin) remains unknown (Shervais & Choi, 2012; Wakabayashi & Dilek, 2000).

Granulite-facies metamorphism was followed by a blueschist-facies event, estimated to occur at 420°C –1.7 GPa, that is, at greater depths and along a much colder thermal gradient. While similar counterclockwise P - T path are frequently recorded during the retrogression of Franciscan eclogite- and amphibolite-facies blocks (e.g., Tsujimori et al., 2006; Wakabayashi, 1990, but not in all blocks, e.g., Mulcahy et al., 2018; Rutte et al., 2020) and observed in other (but not all) metamorphic soles (see review in Wakabayashi and Shimabukuro (2022), and the Turkey example in Dilek and Whitney (1997) and Plunder et al. (2016)), reaching higher pressures implies that either these blocks were never detached from the slab when the subduction progressively cooled, or that they were detached, yet entrained to depth by the underlying slab as a coherent sheet or within a low-viscosity subduction channel. In all cases, the blueschist-facies event likely occurred later than ~ 165 Ma, since it occurred below the amphibole argon closure temperature (Harrison, 1981). Other blocks experienced only blueschist-facies metamorphism (Figure 5j; as observed in Shervais et al. (2011)), without any granulite-facies metamorphism. Although no precise P - T estimates or dating was performed on these rocks, we expect them to form later than the amphibolite, when the subduction thermal gradient gets colder and reaches a more mature state.

The thermal regime is, however, dictated by changes in the subduction thermal conditions, involving subduction speed and the age of the incoming plate (Kirby et al., 1991), such that a steady state may never be reached. In the SMVC area, the Franciscan nappe-stack was mainly assembled in-sequence (Figure 9e), with peak metamorphic temperatures decreasing downwards (and with advancing time; Figure 10c), in line with the downward/oceanward decrease of metamorphic grade previously reported in the Franciscan complex (Ernst, 1971). Yet, the evolution of the thermal gradient (Figure 10d) shows a more complex evolution, with a strong decrease from $\sim 800^{\circ}\text{C/GPa}$ to $\sim 200^{\circ}\text{C/GPa}$ in ~ 15 My during subduction initiation (Anczkiewicz et al., 2004; Cooper et al., 2011) marking the progressive thermal equilibration reaching a mature thermal regime (Soret et al., 2022). Warm metamorphic gradients (up to $\sim 1000^{\circ}\text{C/GPa}$) recorded in the Marin Headlands and the Coastal Belt are associated to shallow depth of underplating (above 10 km). Rather than reflecting a warming of the subduction zone with time, this might be due to a non-linear subduction gradient that is hotter at shallow depth (e.g., Peacock, 1996).

8.3.2. Subduction of a Major Transform Fault and Impacts on Arc Magmatism

Large variations of the age of subducting MORB lithosphere have been highlighted in several studies of the Franciscan complex (Murchey & Blake, 1993; Wakabayashi, 2015, 2017b), showing in particular an abrupt transition from young to old subducting lithosphere around 120 Ma (Figure 10e). Several studies suggest a close approach of the ridge to the trench, or even ridge subduction prior to 120 Ma; Shervais (2001) and Shervais et al. (2004) even propose ridge subduction to explain late MORB magmatism in the Coast Range ophiolite, likely occurring after 150 Ma. This is supported by the young age (~ 20 Ma) at subduction of the first major accreted portion of ocean floor, the South Fork Mountain Schist (containing MORB basalt, Ghatak et al., 2012; Wakabayashi et al., 2010; erupted before 137 Ma, and metamorphosed at 121 Ma; Dumitru et al., 2010, and references therein), and associated relatively warm metamorphic gradient (Wakabayashi, 2015). The main portion of accreted subducting crust after 120 Ma is the Yolla Bolly terrane (~ 60 Ma at subduction). A significant age offset of approximately 40 My in the oceanic crust entering the trench is also necessary to enable the

eruption of the Snow Mountain volcanic complex on the older oceanic lithosphere of the Farallon Plate. Such an offset could only be accommodated by a large transform fault oblique to the trench, of the scale of the present-day Romanche Fault (45 My offset) in the Atlantic Ocean. Assuming the existence of such a transform fault (and possibly other ones subducted at ~105 Ma and ~90 Ma) is an alternative to ridge subduction (that would have a very strong impact on the geological record) and allows a relatively simple kinematic evolution of Farallon-North American plates convergence, with almost constant convergence speed and direction during the whole length of subduction.

A turning point for the accretionary dynamics of the Franciscan complex at ca. 120 Ma is also supported by two main arguments: (a) a change in accretion dynamics and (b) a change in arc activity.

The change in accretion dynamics is evidenced by the fact that few Franciscan units subducted before 123 Ma have been recovered in the Franciscan complex, which is generally interpreted as a period of basal erosion (potentially controlled by seamount subduction, such as recorded above the SMVC) or non-accretion. In turn, major accretion events are recorded between ~120 and ~80 Ma (Apen et al., 2021; Dumitru et al., 2010). Our study is consistent with the general trend, with only small volumes (units above the SMVC) subducted before 120 Ma preserved, and large volumes including the SMVC and units below it after 120 Ma.

The change in arc activity is evidenced by the existence of two main pulses of magmatic activity in the Sierra Nevada: a middle-late Jurassic pulse, and a “mid-Cretaceous” pulse (Chen & Moore, 1982). A correlation emerges between these pulses and the main accretion period (Figure 10f; e.g., Apen et al., 2021; Dumitru et al., 2015). A few striking characteristics emerge: (a) the Jurassic and Cretaceous magmatic pulses correlate with peak metamorphic ages of high-grade blocks in the Franciscan complex and sedimentary-dominated terrane accretion in the Franciscan and the Cretaceous magmatic pulse, respectively, (b) the Early Jurassic and Early Cretaceous magmatic lulls of the Sierra Nevada correspond to periods from which few/no subducted material has been recovered. In the following, we propose a simple model to explain this correlation.

1. Subduction of hydrated mantle along transform faults: serpentine breakdown reactions release large amounts of water from the slab at subarc depth (Schmidt & Poli, 1998; Ulmer & Trommsdorff, 1995). Hence, the extent of seafloor serpentinization exerts a first order control on arc magmatism. In this regard, the subduction of deeply-hydrated lithosphere around transform faults (Prigent et al., 2020) is relevant and may explain magmatic flare-ups in arcs.
2. Arc activity drives the sediment input: the sediment input in the wedge is directly controlled by the activity of the arc, as suggested by the strong affinity of detrital zircon ages with arc magmatic ages underlined by Dumitru et al. (2015) and Apen et al. (2021). Sediment input also strongly depends on the age of the incoming plate (Figure 10e).
3. Thick sediment input enhances underplating (e.g., Cubas et al., 2022; Shreve & Cloos, 1986).
4. Subducted sediments further contribute to arc activity: the metamorphism of sediments also contributes to water release in subduction zone, leading to more arc activity (e.g., Hacker, 2008).

In the Late Cretaceous, arc magmatism in the Sierra Nevada ceased, migrating eastward to the Idaho batholith. This cessation is commonly attributed to slab flattening during the Laramide orogeny (Coney & Reynolds, 1977; English & Johnston, 2004). Some authors posit that the subduction of an oceanic plateau could have triggered this flat slab event (Liu et al., 2010; Livaccari et al., 1981; Tarduno et al., 1985), which makes the geological record of subducted bathymetric anomalies even more relevant.

9. Conclusions

The nappe-stack around the Snow Mountain area allows to study processes associated with seamount subduction, as well as the long-term evolution of the Franciscan subduction complex.

1. The SMVC erupted as an alkaline seamount volcano at ~166 Ma. This seamount was subducted after ~118 Ma, and partially metamorphosed at conditions of ~0.6 GPa, 240°C (i.e., depths of ~20–25 km). Subduction was likely associated with tectonic erosion of the accretionary preexisting wedge, until downward migration of the subduction interface allowed decapitation from the downgoing plate, facilitated by a weak layer of sediments at the base of the unit. Despite no direct evidence for seismic activity, episodic fluid release from metabasalts may have influenced the seismic cycle or shallow slow-slip events. Similar field examples in

- the Franciscan suggest that the decapitation and exhumation of subducted seamounts was probably more common than assumed.
2. Amphibolite-facies blocks with supra-subduction-zone signatures included in a serpentinite mélangé on top of the nappe-stack were metamorphosed at ~1 GPa, 800°C during subduction infancy (~170 Ma). Later metamorphism occurred on a much colder thermal gradient, both at the local and regional scales, which hints to thermal maturation of the subduction zone over ~10 My.
 3. Abrupt temporal variations in the age of the oceanic plate entering the trench suggest the subduction of large-offset transform faults. This may have affected sediment input in the trench as well as magmatic flare-ups and erosion in the Sierra Nevada arc.

Data Availability Statement

All data are available at <https://zenodo.org/deposit/8211909>. This includes: (a) Sample location. (b) Bulk-rock analyses. (c) Synthesis of EPMA data. (d) Synthesis of RSCM temperatures. (e) Titanite U-Pb-trace element data. (D6) Zircon U-Pb-trace element data (Bonnet et al., 2024).

Acknowledgments

The authors are grateful to the USDA Forest Service and Stonyford ranger station for granting permission to access the Snow Mountain Wilderness during the Ranch Fire closure, and forest geologist R. Mikulowsky for his help in planning fieldwork. Financial resources for this study were provided by the NSF partnership for international research and education EFIRE (OIA 1545903), with additional funding from UCSB, NSF, and ISTeP. The authors are thankful to P. Maffre, a dedicated field assistant, and to B.R. Hacker for constructive remarks on an early version of this manuscript and overall support. E. Delairis is acknowledged for thin section preparation, and N. Rividi and M. Fialin for their help with EPMA analyses. The authors thank C. Chauvel for providing Pb isotope reference material. Additional thanks go to editor M. Rusmore, associate editor F. Rossetti, and reviewers J. Wakabayashi and G. Vignaroli whose comments led to significant improvements. Open access funding provided by Universitat Bern.

References

- Agard, P., Plunder, A., Angiboust, S., Bonnet, G., & Ruh, J. B. (2018). The subduction plate interface: Rock record and mechanical coupling (from long to short timescales). *Lithos*, 320–321, 537–566. <https://doi.org/10.1016/j.lithos.2018.09.029>
- Agard, P., Prigent, C., Soret, M., Dubacq, B., Guillot, S., & Deldicque, D. (2020). Slabification: Mechanisms controlling subduction development and viscous coupling. *Earth-Science Reviews*, 208, 103259. <https://doi.org/10.1016/j.earscirev.2020.103259>
- Agard, P., Soret, M., Bonnet, G., Ninkabou, D., Plunder, A., Prigent, C., & Yamato, P. (2023). Subduction and obduction processes: The fate of oceanic lithosphere revealed by blueschists, eclogites, and ophiolites. In *Compressional Tectonics: Plate Convergence to Mountain Building*, *Geophysical Monograph*. American Geophysical Union.
- Albarède, F., & Tamagnan, V. (1988). Modelling the recent geochemical evolution of the Piton de la Fournaise volcano, Réunion Island, 1931–1986. *Journal of Petrology*, 29(5), 997–1030. <https://doi.org/10.1093/petrology/29.5.997>
- Anczkiewicz, R., Platt, J. P., Thirlwall, M. F., & Wakabayashi, J. (2004). Franciscan subduction off to a slow start: Evidence from high-precision Lu-Hf garnet ages on high grade-blocks. *Earth and Planetary Science Letters*, 225(1–2), 147–161. <https://doi.org/10.1016/j.epsl.2004.06.003>
- Apen, F. E., Wakabayashi, J., Day, H. W., Roeske, S. M., Souders, A. K., & Dumitru, T. A. (2021). Regional-scale correlations of accreted units in the Franciscan Complex, California, USA: A record of long-lived, episodic subduction accretion. *Plate Tectonics, Ophiolites, and Societal Significance of Geology: A Celebration of the Career of Eldridge Moores* (pp. 233–255). [https://doi.org/10.1130/2021.2552\(11\)](https://doi.org/10.1130/2021.2552(11))
- Arkula, C., Lom, N., Wakabayashi, J., Rea-Downing, G., Qayyum, A., Dekkers, M. J., et al. (2023). The forearc ophiolites of California formed during trench-parallel spreading: Kinematic reconstruction of the western USA Cordillera since the Jurassic. *Earth-Science Reviews*, 237, 104275. <https://doi.org/10.1016/j.earscirev.2022.104275>
- Bagheri, S., & Stampfli, G. M. (2008). The Anarak, Jandaq and Posht-e-Badam metamorphic complexes in central Iran: New geological data, relationships and tectonic implications. *Tectonophysics*, 451(1–4), 123–155. <https://doi.org/10.1016/j.tecto.2007.11.047>
- Bailey, E. H., & Blake, M. C. J. (1974). Major chemical characteristics of Mesozoic Coast Range ophiolite in California. *Journal of Research of the U. S. Geological Survey*, 2, 637–656.
- Barbero, E., Di Rosa, M., Pandolfi, L., Delavari, M., Dolati, A., Zaccarini, F., et al. (2023). Deformation history and processes during accretion of seamounts in subduction zones: The example of the Durkan Complex (Makran, SE Iran). *Geoscience Frontiers*, 14(2), 101522. <https://doi.org/10.1016/j.gsf.2022.101522>
- Barbero, E., Pandolfi, L., Delavari, M., Dolati, A., Saccani, E., Catanzariti, R., et al. (2021). The western Durkan Complex (Makran Accretionary Prism, SE Iran): A Late Cretaceous tectonically disrupted seamounts chain and its role in controlling deformation style. *Geoscience Frontiers*, 12(3), 101106. <https://doi.org/10.1016/j.gsf.2020.12.001>
- Barth, A. P., & Wooden, J. L. (2006). Timing of magmatism following initial convergence at a Passive margin, Southwestern U.S. Cordillera, and ages of lower crustal magma sources. *The Journal of Geology*, 114(2), 231–245. <https://doi.org/10.1086/499573>
- Barth, A. P., Wooden, J. L., Howard, K. A., & Richards, J. L. (2008). Late Jurassic plutonism in the southwest U.S. Cordillera. In *Special Paper 438: Ophiolites, Arcs, and Batholiths: A Tribute to Cliff Hopson* (pp. 379–396). Geological Society of America. [https://doi.org/10.1130/2008.2438\(13\)](https://doi.org/10.1130/2008.2438(13))
- Bebout, G. E., & Penniston-Dorland, S. C. (2016). Fluid and mass transfer at subduction interfaces - The field metamorphic record. *Lithos*, 240–243, 228–258. <https://doi.org/10.1016/j.lithos.2015.10.007>
- Belgrano, T. M., Diamond, L. W., Vogt, Y., Biedermann, A. R., Gilgen, S. A., & Al-Tobi, K. (2019). A revised map of volcanic units in the Oman ophiolite: Insights into the architecture of an oceanic proto-arc volcanic sequence. *Solid Earth*, 10(4), 1181–1217. <https://doi.org/10.5194/se-10-1181-2019>
- Berkland, J. O. (1978). Franciscan Complex - Great Valley Sequence relationships North of Clear Lake, California. *Castle Steam Field, Great Valley Sequence*, 9–25.
- Blake, M. C., Jr., Howell, D. G., & Jayko, A. S. (1984). Tectonostratigraphic terranes of the San Francisco Bay Region. In *Franciscan Geology of Northern California, Pacific Section SEPM* (pp. 5–22).
- Bonnet, G., Agard, P., Angiboust, S., Fournier, M., & Omrani, J. (2019). No large earthquakes in fully exposed subducted seamount. *Geology*, 47(5), 407–410. <https://doi.org/10.1130/G45564.1>
- Bonnet, G., Agard, P., Angiboust, S., Monié, P., Fournier, M., Caron, B., & Omrani, J. (2019). Structure and metamorphism of a subducted seamount (Zagros suture, Southern Iran). *Geosphere*, 15(1), 62–81. <https://doi.org/10.1130/GES02134.1>
- Bonnet, G., Agard, P., Whitechurch, H., Fournier, M., Angiboust, S., Caron, B., & Omrani, J. (2020). Fossil seamount in SE Zagros records intraoceanic arc to back-arc transition: New constraints for the evolution of the Neotethys. *Gondwana Research*, 81, 423–444. <https://doi.org/10.1016/j.gr.2019.10.019>

- Bonnet, G., Apen, F. E., Soret, M., Noël, J., Caron, B., Ninkabou, D., et al. (2024). Seamount subduction dynamics and long-term evolution of the Franciscan active margin [Dataset]. *Zenodo*. <https://zenodo.org/doi/10.5281/zenodo.8211908>
- Brown, R. D. (1964). Geologic map of the Stonyford quadrangle, Glenn, Colusa, and Lake counties, California. *US Geological Survey Mineral Investigations Filed Studies Map MF-279*. scale 1:48 000.
- Chen, J. H., & Moore, J. G. (1982). Uranium-lead isotopic ages from the Sierra Nevada Batholith, California. *Journal of Geophysical Research*, 87(B6), 4761–4784. <https://doi.org/10.1029/JB087iB06p04761>
- Choi, S. H., Mukasa, S. B., & Shervais, J. W. (2008). Initiation of Franciscan subduction along a large-offset fracture zone: Evidence from mantle peridotites, Stonyford, California. *Geology*, 36(8), 595. <https://doi.org/10.1130/G24993A.1>
- Cloos, M., & Shreve, R. L. (1996). Shear zone thickness and the seismicity of Chilean- and Mariana-type subduction zones. *Geology*, 24(2), 107–110. [https://doi.org/10.1130/0091-7613\(1996\)024<0107:SZTATS>2.3.CO;2](https://doi.org/10.1130/0091-7613(1996)024<0107:SZTATS>2.3.CO;2)
- Condit, C. B., Guevara, V. E., Delph, J. R., & French, M. E. (2020). Slab dehydration in warm subduction zones at depths of episodic slip and tremor. *Earth and Planetary Science Letters*, 552, 116601. <https://doi.org/10.1016/j.epsl.2020.116601>
- Coney, P. J., & Reynolds, S. J. (1977). Cordilleran Benioff zones. *Nature*, 270(5636), 403–406. <https://doi.org/10.1038/270403a0>
- Cooper, F. J., Platt, J. P., & Anczkiewicz, R. (2011). Constraints on early Franciscan subduction rates from 2-D thermal modeling. *Earth and Planetary Science Letters*, 312(1–2), 69–79. <https://doi.org/10.1016/j.epsl.2011.09.051>
- Cubas, N., Agard, P., & Tissandier, R. (2022). Earthquake ruptures and topography of the Chilean margin controlled by plate interface deformation. *Solid Earth*, 13(3), 779–792. <https://doi.org/10.5194/se-13-779-2022>
- Dal Zilio, L., & Gerya, T. (2022). Subduction earthquake cycles controlled by episodic fluid pressure cycling. *Lithos*, 426–427, 106800. <https://doi.org/10.1016/j.lithos.2022.106800>
- Dewey, J. F., & Bird, J. M. (1971). Origin and emplacement of the ophiolite suite: Appalachian ophiolites in Newfoundland. *Journal of Geophysical Research*, 76(14), 3179–3206. <https://doi.org/10.1029/JB076i014p03179>
- Dickinson, W. R. (1970). Relations of andesites, granites, and derivative sandstones to arc-Trench tectonics. *Reviews of Geophysics*, 8(4), 813–860. <https://doi.org/10.1029/RG008i004p00813>
- Diener, J. F. A., & Powell, R. (2012). Revised activity-composition models for clinopyroxene and amphibole. *Journal of Metamorphic Geology*, 30(2), 131–142. <https://doi.org/10.1111/j.1525-1314.2011.00959.x>
- Dilek, Y., & Whitney, D. L. (1997). Counterclockwise *P-T-t* trajectory from the metamorphic sole of a Neo-Tethyan ophiolite (Turkey). *Tectonophysics*, 280(3–4), 295–310. [https://doi.org/10.1016/S0040-1951\(97\)00038-3](https://doi.org/10.1016/S0040-1951(97)00038-3)
- Dominguez, S., Lallemand, S. E., Malavieille, J., & von Huene, R. (1998). Upper plate deformation associated with seamount subduction. *Tectonophysics*, 293(3–4), 207–224. [https://doi.org/10.1016/S0040-1951\(98\)00086-9](https://doi.org/10.1016/S0040-1951(98)00086-9)
- Dumitru, T. A., Ernst, W. G., Hourigan, J. K., & McLaughlin, R. J. (2015). Detrital zircon U–Pb reconnaissance of the Franciscan subduction complex in northwestern California. *International Geology Review*, 57(5–8), 767–800. <https://doi.org/10.1080/00206814.2015.1008060>
- Dumitru, T. A., Ernst, W. G., Wright, J. E., Wooden, J. L., Wells, R. E., Farmer, L. P., et al. (2013). Eocene extension in Idaho generated massive sediment floods into the Franciscan trench and into the Tyee, Great Valley, and Green River basins. *Geology*, 41(2), 187–190. <https://doi.org/10.1130/G33746.1>
- Dumitru, T. A., Wakabayashi, J., Wright, J. E., & Wooden, J. L. (2010). Early Cretaceous transition from nonaccretionary behavior to strongly accretionary behavior within the Franciscan subduction complex. *Tectonics*, 29(5), TC5001. <https://doi.org/10.1029/2009TC002542>
- Embley, R. W., & Rubin, K. H. (2018). Extensive young silicic volcanism produces large deep submarine lava flows in the NE Lau Basin. *Bulletin of Volcanology*, 80(4), 36. <https://doi.org/10.1007/s00445-018-1211-7>
- English, J. M., & Johnston, S. T. (2004). The Laramide orogeny: What were the driving forces? *International Geology Review*, 46(9), 833–838. <https://doi.org/10.2747/0020-6814.46.9.833>
- Ernst, W. G. (1970). Tectonic contact between the Franciscan mélange and the Great Valley sequence-crustal expression of a late Mesozoic Benioff zone. *Journal of Geophysical Research*, 75(5), 886–901. <https://doi.org/10.1029/JB075i005p00886>
- Ernst, W. G. (1971). Metamorphic zonations on presumably subducted lithospheric plates from Japan, California and the Alps. *Contributions to Mineralogy and Petrology*, 34(1), 43–59. <https://doi.org/10.1007/BF00376030>
- Ernst, W. G., & McLaughlin, R. J. (2012). Mineral parageneses, regional architecture, and tectonic evolution of Franciscan metagraywackes, Cape Mendocino-Garberville-Covelo 30' × 60' quadrangles, northwest California. *Tectonics*, 31(1), TC1001. <https://doi.org/10.1029/2011TC002987>
- Etnoyer, P. J., Wood, J., & Shirley, T. C. (2010). Box 12: How large is the seamount biome. *Oceanography*, 23(01), 206–209. <https://doi.org/10.5670/oceanog.2010.96>
- Ghatak, A., Basu, A. R., & Wakabayashi, J. (2012). Elemental mobility in subduction metamorphism: Insight from metamorphic rocks of the Franciscan Complex and the Feather River ultramafic belt, California. *International Geology Review*, 54(6), 654–685. <https://doi.org/10.1080/00206814.2011.567087>
- Gillet, P., & Goffé, B. (1988). On the significance of aragonite occurrences in the Western Alps. *Contributions to Mineralogy and Petrology*, 99(1), 70–81. <https://doi.org/10.1007/BF00399367>
- Giuntoli, F., & Viola, G. (2022). A likely geological record of deep tremor and slow slip events from a subducted continental broken formation. *Scientific Reports*, 12(1), 4506. <https://doi.org/10.1038/s41598-022-08489-2>
- Got, J.-L., Monteiller, V., Monteux, J., Hassani, R., & Okubo, P. (2008). Deformation and rupture of the oceanic crust may control growth of Hawaiian volcanoes. *Nature*, 451(7177), 453–456. <https://doi.org/10.1038/nature06481>
- Guilmette, C., Hébert, R., Dostal, J., Indares, A., Ullrich, T., Bédard, É., & Wang, C. (2012). Discovery of a dismembered metamorphic sole in the Saga ophiolitic mélange, South Tibet: Assessing an Early Cretaceous disruption of the Neo-Tethyan supra-subduction zone and consequences on basin closing. *Gondwana Research*, 22(2), 398–414. <https://doi.org/10.1016/j.gr.2011.10.012>
- Guilmette, C., Smit, M. A., van Hinsbergen, D. J. J., Gürer, D., Corfu, F., Charette, B., et al. (2018). Forced subduction initiation recorded in the sole and crust of the Semail Ophiolite of Oman. *Nature Geoscience*, 11(9), 688–695. <https://doi.org/10.1038/s41561-018-0209-2>
- Hacker, B. R. (2008). H₂O subduction beyond arcs. *Geochemistry, Geophysics, Geosystems*, 9(3), Q03001. <https://doi.org/10.1029/2007gc001707>
- Harrison, T. M. (1981). Diffusion of ⁴⁰Ar in hornblende. *Contributions to Mineralogy and Petrology*, 78, 324–331. <https://doi.org/10.1007/BF00398927>
- Hart, S. R. (1984). A large-scale isotope anomaly in the Southern Hemisphere mantle. *Nature*, 309(5971), 753–757. <https://doi.org/10.1038/309753a0>
- Hayden, L. A., Watson, E. B., & Wark, D. A. (2008). A thermobarometer for sphene (titanite). *Contributions to Mineralogy and Petrology*, 155(4), 529–540. <https://doi.org/10.1007/s00410-007-0256-y>

- Hervieu, C., Agard, P., Verlaquet, A., Gyonlai, T., Bonnet, G., Mendes, K., & Plunder, A. (2023). Fractal distribution of subduction-related crack-seal veins (Schistes Lustrés, W. Alps): Implications for fluid flow and rupture processes at the downdip end of the seismogenic zone. *Journal of Geophysical Research: Solid Earth*, 128(10), e2022JB026317. <https://doi.org/10.1029/2022jb026317>
- Hopson, C. A., Mattinson, J. M., Pessagno, E. A., & Luyendyk, B. P. (2008). California Coast Range ophiolite: Composite Middle and Late Jurassic oceanic lithosphere. In *Special Paper 438: Ophiolites, Arcs, and Batholiths: A Tribute to Cliff Hopson* (pp. 1–101). Geological Society of America. [https://doi.org/10.1130/2008.2438\(01\)](https://doi.org/10.1130/2008.2438(01))
- Hopson, C. A., & Pessagno, E. A. (2005). Tehama-Colusa serpentinite mélange: A remnant of Franciscan Jurassic oceanic lithosphere, northern California. *International Geology Review*, 47(1), 65–100. <https://doi.org/10.2747/0020-6814.47.1.65>
- Hosokawa, T., & Hashimoto, Y. (2022). Geological constraints on dynamic changes of fluid pressure in seismic cycles. *Scientific Reports*, 12(1), 14789. <https://doi.org/10.1038/s41598-022-19083-x>
- Huot, F., & Maury, R. C. (2002). The Round Mountain serpentinite mélange, northern Coast Ranges of California: An association of backarc and arc-related tectonic units. *Geological Society of America Bulletin*, 114(1), 109–123. [https://doi.org/10.1130/0016-7606\(2002\)114<0109:TRMSML>2.0.CO;2](https://doi.org/10.1130/0016-7606(2002)114<0109:TRMSML>2.0.CO;2)
- Hyndman, R. D., Yamano, M., & Oleskevich, D. A. (1997). The seismogenic zone of subduction thrust faults. *Island Arc*, 6(3), 244–260. <https://doi.org/10.1111/j.1440-1738.1997.tb00175.x>
- Ide, S., Beroza, G. C., Shelly, D. R., & Uchide, T. (2007). A scaling law for slow earthquakes. *Nature*, 447(7140), 76–79. <https://doi.org/10.1038/nature05780>
- Jackson, M. G., & Dasgupta, R. (2008). Compositions of HIMU, EM1, and EM2 from global trends between radiogenic isotopes and major elements in ocean island basalts. *Earth and Planetary Science Letters*, 276(1–2), 175–186. <https://doi.org/10.1016/j.epsl.2008.09.023>
- Kelleher, J., & McCann, W. (1976). Buoyant zones, great earthquakes, and unstable boundaries of subduction. *Journal of Geophysical Research*, 81(26), 4885–4896. <https://doi.org/10.1029/JB081i026p04885>
- Kirby, S. H., Durham, W. B., & Stern, L. A. (1991). Mantle phase changes and deep-earthquake faulting in subducting lithosphere. *Science*, 252(5003), 216–225. <https://doi.org/10.1126/science.252.5003.216>
- Kirkpatrick, J. D., & Rowe, C. D. (2013). Disappearing ink: How pseudotachylites are lost from the rock record. *Journal of Structural Geology*, 52, 183–198. <https://doi.org/10.1016/j.jsg.2013.03.003>
- Kuno, H. (1968). Differentiation of basaltic magmas. In *The Poldervaart Treatise on rocks of basaltic composition* (pp. 623–688). Interscience Publishers.
- Lahfid, A., Beyssac, O., Deville, E., Negro, F., Chopin, C., & Goffé, B. (2010). Evolution of the Raman spectrum of carbonaceous material in low-grade metasediments of the Glarus Alps (Switzerland). *Terra Nova*, 22(5), 354–360. <https://doi.org/10.1111/j.1365-3121.2010.00956.x>
- Lallemant, S., Peyret, M., van Rijsingen, E., Arcay, D., & Heuret, A. (2018). Roughness characteristics of oceanic seafloor prior to subduction in relation to the seismogenic potential of subduction zones. *Geochemistry, Geophysics, Geosystems*, 19(7), 2121–2146. <https://doi.org/10.1029/2018GC007434>
- Lallemant, S. E., Schnürle, P., & Malavieille, J. (1994). Coulomb theory applied to accretionary and nonaccretionary wedges: Possible causes for tectonic erosion and/or frontal accretion. *Journal of Geophysical Research*, 99(B6), 12033–12055. <https://doi.org/10.1029/94JB00124>
- Larue, D. K., Barnes, I., & Sedlock, R. L. (1989). Subduction and accretion of the Permanente terrane near San Francisco, California. *Tectonics*, 8(2), 221–235. <https://doi.org/10.1029/TC008i002p00221>
- Le Bas, M. J., Maitre, R. W. L., Streckeisen, A., Zanettin, B., & IUGS Subcommittee on the Systematics of Igneous Rocks. (1986). A chemical classification of volcanic rocks based on the total alkali-silica diagram. *Journal of Petrology*, 27(3), 745–750. <https://doi.org/10.1093/petrology/27.3.745>
- Liao, Y., Wei, C., & Rehman, H. U. (2021). Titanium in calcium amphibole: Behavior and thermometry. *American Mineralogist*, 106(2), 180–191. <https://doi.org/10.2138/am-2020-7409>
- Liu, L., Gurnis, M., Seton, M., Saleeby, J. B., Müller, R. D., & Jackson, J. M. (2010). The role of oceanic plateau subduction in the Laramide orogeny. *Nature Geoscience*, 3(5), 353–357. <https://doi.org/10.1038/ngeo829>
- Livaccari, R. F., Burke, K., & Şengör, A. M. C. (1981). Was the Laramide orogeny related to subduction of an oceanic plateau? *Nature*, 289(5795), 276–278. <https://doi.org/10.1038/289276a0>
- MacPherson, G. J. (1981). *Geology and petrology of the Mesozoic submarine volcanic complex at Snow Mountain, northern Coast Ranges, California: An onland seamount* (Unpublished Ph.D. dissertation). Princeton University.
- MacPherson, G. J. (1983). The Snow Mountain volcanic complex: An on-land seamount in the Franciscan terrain, California. *The Journal of Geology*, 91(1), 73–92. <https://doi.org/10.1086/628745>
- MacPherson, G. J., & Phipps, S. P. (1985). Comment on “Geochemical evidence for the tectonic setting of the Coast Range ophiolite: A composite island arc–oceanic crust terrane in western California”. *Geology*, 13(11), 827. [https://doi.org/10.1130/0091-7613\(1985\)13<827:CAROGE>2.0.CO;2](https://doi.org/10.1130/0091-7613(1985)13<827:CAROGE>2.0.CO;2)
- MacPherson, G. J., Phipps, S. P., & Grossman, J. N. (1990). Diverse sources for igneous blocks in Franciscan melanges, California Coast Ranges. *The Journal of Geology*, 98(6), 845–862. <https://doi.org/10.1086/629457>
- Mankinen, E. A., Gromme, C. S., & Williams, K. M. (1991). Concordant paleolatitudes from ophiolite sequences in the northern California Coast Ranges, USA. *Tectonophysics*, 198, 1–21. [https://doi.org/10.1016/0040-1951\(91\)90127-E](https://doi.org/10.1016/0040-1951(91)90127-E)
- Maruyama, S., & Liou, J. G. (1988). Petrology of Franciscan metabasites along the jadeite-glaucophane type facies series, Cazadero, California. *Journal of Petrology*, 29, 1–37. <https://doi.org/10.1093/petrology/29.1.1>
- Maruyama, S., & Liou, J. G. (1989). Possible depth limit for underplating by a seamount. *Tectonophysics*, 160(1–4), 327–337. [https://doi.org/10.1016/0040-1951\(89\)90399-5](https://doi.org/10.1016/0040-1951(89)90399-5)
- McDonough, W. F., & Sun, S. S. (1995). The composition of the Earth. *Chemical Geology*, 120(3–4), 223–253. [https://doi.org/10.1016/0009-2541\(94\)00140-4](https://doi.org/10.1016/0009-2541(94)00140-4)
- McLaughlin, R. J., Blake, M. C., Griscorn, A., Blome, C. D., & Murchey, B. (1988). Tectonics of formation, translation, and dispersal of the Coast Range Ophiolite of California. *Tectonics*, 7(5), 1033–1056. <https://doi.org/10.1029/TC007i005p01033>
- Meneghini, F., & Moore, J. C. (2007). Deformation and hydrofracture in a subduction thrust at seismogenic depths: The Rodeo Cove thrust zone, Marin Headlands, California. *Geological Society of America Bulletin*, 119(1–2), 174–183. <https://doi.org/10.1130/B25807.1>
- Moore, J. G. (1965). Petrology of deep-sea basalt near Hawaii. *American Journal of Science*, 5(1), 40–52. <https://doi.org/10.2475/ajs.263.1.40>
- Mulcahy, S. R., Starnes, J. K., Day, H. W., Coble, M. A., & Vervoort, J. D. (2018). Early Onset of Franciscan subduction. *Tectonics*, 37(5), 1194–1209. <https://doi.org/10.1029/2017TC004753>
- Müller, R. D., Cannon, J., Qin, X., Watson, R. J., Gurnis, M., Williams, S., et al. (2018). GPlates: Building a Virtual Earth through deep time. *Geochemistry, Geophysics, Geosystems*, 19(7), 2243–2261. <https://doi.org/10.1029/2018GC007584>

- Munoz-Montecinos, J., Cambeses, A., & Angiboust, S. (2023). Accretion and subduction mass transfer processes: Zircon SHRIMP and geochemical insights from the Carboniferous Western Series, Central Chile. *International Geology Review*, 66, 1–27. <https://doi.org/10.1080/00206814.2023.2185822>
- Murchev, B. L., & Blake, M. C., Jr. (1993). Evidence for subduction of a major ocean plate along the California margin during the Middle to Early Late Jurassic. In *Mesozoic Paleogeography of the Western United States-II, Pacific Section SEPM* (pp. 1–18).
- Murchev, B. L., & Jones, D. L. (1984). Age and significance of chert in the Franciscan complex in the San Francisco Bay region. In *Franciscan Geology of Northern California, Pacific Section SEPM* (pp. 23–30).
- Nakamura, Y., Yoshino, T., & Satish-Kumar, M. (2017). An experimental kinetic study on the structural evolution of natural carbonaceous material to graphite. *American Mineralogist*, 102(1), 135–148. <https://doi.org/10.2138/am-2017-5733>
- Needy, S. K., Anderson, J. L., Wooden, J. L., Fleck, R. J., Barth, A. P., Paterson, S. R., et al. (2009). Mesozoic magmatism in an upper- to middle-crustal section through the Cordilleran continental margin arc, eastern Transverse Ranges, California. In *Crustal Cross Sections from the Western North American Cordillera and Elsewhere: Implications for Tectonic and Petrologic Processes*. Geological Society of America. [https://doi.org/10.1130/2009.2456\(07\)](https://doi.org/10.1130/2009.2456(07))
- Nicolas, A. (2000). Accretion of Oman and United Arab Emirates ophiolite – Discussion of a new structural map. *Marine Geophysical Researches*, 21(3/4), 147–180. <https://doi.org/10.1023/A:1026769727917>
- Niemeijer, A. R., & Spiers, C. J. (2005). Influence of phyllosilicates on fault strength in the brittle-ductile transition: Insights from rock analogue experiments. *Geological Society, London, Special Publications*, 245(1), 303–327. <https://doi.org/10.1144/GSL.SP.2005.245.01.15>
- Noda, A., Koge, H., Yamada, Y., Miyakawa, A., & Ashi, J. (2020). Subduction of trench-fill sediments beneath an accretionary wedge: Insights from sandbox analogue experiments. *Geosphere*, 16(4), 953–968. <https://doi.org/10.1130/GES02212.1>
- Orme, D. A., & Surpless, K. D. (2019). The birth of a forearc: The basal Great Valley Group, California, USA. *Geology*, 47(8), 757–761. <https://doi.org/10.1130/G46283.1>
- Pattison, D. R. M., De Capitani, C., & Gaidies, F. (2011). Petrological consequences of variations in metamorphic reaction affinity. *Journal of Metamorphic Geology*, 29(9), 953–977. <https://doi.org/10.1111/j.1525-1314.2011.00950.x>
- Peacock, S. M. (1996). Thermal and petrologic structure of subduction zones. In *Subduction: Top to bottom* (pp. 119–133). <https://doi.org/10.1029/GM096p0119>
- Pearce, J. A. (1996). A user's guide to basalt discrimination diagrams. In *Trace Element Geochemistry of Volcanic Rocks: Applications for Massive Sulphide Exploration* (pp. 79–113). Geological Association of Canada, Short Course Notes.
- Pearce, J. A. (2008). Geochemical fingerprinting of oceanic basalts with applications to ophiolite classification and the search for Archean oceanic crust. *Lithos*, 100(1–4), 14–48. <https://doi.org/10.1016/j.lithos.2007.06.016>
- Plank, T., & Langmuir, C. H. (1998). The chemical composition of subducting sediment and its consequences for the crust and mantle. *Chemical Geology*, 145(3–4), 325–394. [https://doi.org/10.1016/S0009-2541\(97\)00150-2](https://doi.org/10.1016/S0009-2541(97)00150-2)
- Plunder, A., Agard, P., Chopin, C., Pourteau, A., & Okay, A. I. (2015). Accretion, underplating and exhumation along a subduction interface: From subduction initiation to continental subduction (Tavsanli zone, W. Turkey). *Lithos*, 226, 233–254. <https://doi.org/10.1016/j.lithos.2015.01.007>
- Plunder, A., Agard, P., Chopin, C., Soret, M., Okay, A. I., & Whitechurch, H. (2016). Metamorphic sole formation, emplacement and blueschist-facies overprint: Early subduction dynamics witnessed by western Turkey ophiolites. *Terra Nova*, 28(5), 329–339. <https://doi.org/10.1111/ter.12225>
- Pourteau, A., Scherer, E. E., Schorn, S., Bast, R., Schmidt, A., & Ebert, L. (2019). Thermal evolution of an ancient subduction interface revealed by Lu–Hf garnet geochronology, Halilbağ Complex (Anatolia). *Geoscience Frontiers*, 10(1), 127–148. <https://doi.org/10.1016/j.gsf.2018.03.004>
- Prigent, C., Agard, P., Guillot, S., Godard, M., & Dubacq, B. (2018). Mantle wedge (de)formation during subduction infancy: Evidence from the base of the Semail ophiolitic mantle. *Journal of Petrology*, 59(11), 2061–2092. <https://doi.org/10.1093/petrology/egy090>
- Prigent, C., Warren, J. M., Kohli, A. H., & Teyssier, C. (2020). Fracture-mediated deep seawater flow and mantle hydration on oceanic transform faults. *Earth and Planetary Science Letters*, 532, 115988. <https://doi.org/10.1016/j.epsl.2019.115988>
- Ranero, C. R., & von Huene, R. (2000). Subduction erosion along the Middle America convergent margin. *Nature*, 404(6779), 748–752. <https://doi.org/10.1038/35008046>
- Ravna, E. J. K., & Terry, M. P. (2004). Geothermobarometry of UHP and HP eclogites and schists - An evaluation of equilibria among garnet-clinopyroxene-kyanite-phengite-coesite/quartz. *Journal of Metamorphic Geology*, 22(6), 579–592. <https://doi.org/10.1111/j.1525-1314.2004.00534.x>
- Regalla, C. A., Rowe, C. D., Harrichhausen, N., Tarling, M. S., & Singh, J. (2018). Styles of underplating in the Marin Headlands terrane, Franciscan complex, California. In *Geology and Tectonics of Subduction Zones: A Tribute to Gaku Kimura*. Geological Society of America. [https://doi.org/10.1130/2018.2534\(10\)](https://doi.org/10.1130/2018.2534(10))
- Ring, U., & Brandon, M. T. (1994). Kinematic data for the Coast Range fault and implications for exhumation of the Franciscan subduction complex. *Geology*, 22(8), 735. [https://doi.org/10.1130/0091-7613\(1994\)022<0735:KDFTCR>2.3.CO;2](https://doi.org/10.1130/0091-7613(1994)022<0735:KDFTCR>2.3.CO;2)
- Ring, U., & Brandon, M. T. (1999). Ductile deformation and mass loss in the Franciscan Subduction Complex: Implications for exhumation processes in accretionary wedges. *Geological Society, London, Special Publications*, 154(1), 55–86. <https://doi.org/10.1144/GSL.SP.1999.154.01.03>
- Rioux, M., Garber, J., Bauer, A., Bowering, S., Searle, M., Kelemen, P., & Hacker, B. (2016). Synchronous formation of the metamorphic sole and igneous crust of the Semail ophiolite: New constraints on the tectonic evolution during ophiolite formation from high-precision U–Pb zircon geochronology. *Earth and Planetary Science Letters*, 451, 185–195. <https://doi.org/10.1016/j.epsl.2016.06.051>
- Rioux, M., Garber, J. M., Searle, M., Crowley, J. L., Stevens, S., Schmitz, M., et al. (2023). The temporal evolution of subduction initiation in the Semail ophiolite: High-precision U–Pb zircon petrochronology of the metamorphic sole. *Journal of Metamorphic Geology*, 41(6), 817–847. <https://doi.org/10.1111/jmg.12719>
- Ruh, J. B., Sallarès, V., Ranero, C. R., & Gerya, T. V. (2017). Crustal deformation dynamics and stress evolution during seamount subduction: High-resolution 3-D numerical modeling. *Journal of Geophysical Research: Solid Earth*, 122, 2069–2084. <https://doi.org/10.1002/2016JB013608>
- Rutte, D., Garber, J., Kylander-Clark, A., & Renne, P. R. (2020). An Exhumation pulse from the nascent Franciscan subduction zone (California, USA). *Tectonics*, 39(10), e2020TC006305. <https://doi.org/10.1029/2020TC006305>
- Saha, A., Basu, A. R., Wakabayashi, J., & Wortman, G. L. (2005). Geochemical evidence for a subducted infant arc in Franciscan high-grade-metamorphic tectonic blocks. *Bulletin of the Geological Society of America*, 117(9), 1318–1335. <https://doi.org/10.1130/B25593.1>
- Schmidt, M. W., & Poli, S. (1998). Experimentally based water budgets for dehydrating slabs and consequences for arc magma generation. *Earth and Planetary Science Letters*, 163(1–4), 361–379. [https://doi.org/10.1016/S0012-821X\(98\)00142-3](https://doi.org/10.1016/S0012-821X(98)00142-3)

- Schmidt, W. L., & Platt, J. P. (2022). Stress, microstructure, and deformation mechanisms during subduction underplating at the depth of tremor and slow slip, Franciscan Complex, northern California. *Journal of Structural Geology*, 154, 104469. <https://doi.org/10.1016/j.jsg.2021.104469>
- Schnur, S. R., & Gilbert, L. A. (2012). Detailed volcanostratigraphy of an accreted seamount: Implications for intraplate seamount formation. *Geochemistry, Geophysics, Geosystems*, 13(12), 1–13. <https://doi.org/10.1029/2012GC004301>
- Scholl, D. W., & Von Huene, R. (2007). Crustal recycling at modern subduction zones applied to the past—Issues of growth and preservation of continental basement crust, mantle geochemistry, and supercontinent reconstruction. In *Geological Society of America Memoirs* (pp. 9–32). Geological Society of America. [https://doi.org/10.1130/2007.1200\(02\)](https://doi.org/10.1130/2007.1200(02))
- Scholz, C. H., & Small, C. (1997). The effect of seamount subduction on seismic coupling. *Geology*, 25(6), 487. [https://doi.org/10.1130/0091-7613\(1997\)025<0487](https://doi.org/10.1130/0091-7613(1997)025<0487)
- Searle, M. P., & Malpas, J. (1980). Structure and metamorphism of rocks beneath the Semail ophiolite of Oman and their significance in ophiolite obduction. *Transactions of the Royal Society of Edinburgh Earth Sciences*, 71(4), 247–262. <https://doi.org/10.1017/S0263593300013614>
- Servais, J. W. (1989). Geochemistry of igneous rocks from the Marin Headlands. In *Geology of San Francisco and Vicinity: 28th International Geological Congress Field Trip Guidebook* (pp. 40–41). American Geophysical Union.
- Servais, J. W. (2001). Birth, death, and resurrection: The life cycle of suprasubduction zone ophiolites. *Geochemistry, Geophysics, Geosystems*, 2(1), 1010. <https://doi.org/10.1029/2000GC000080>
- Servais, J. W. (2022). The petrogenesis of modern and ophiolitic lavas reconsidered: Ti-V and Nb-Th. *Geosci. Frontier Times*, 13(2), 101319. <https://doi.org/10.1016/j.gsf.2021.101319>
- Servais, J. W., & Choi, S. H. (2012). Subduction initiation along transform faults: The proto-Franciscan subduction zone. *Lithosphere*, 4(6), 484–496. <https://doi.org/10.1130/L153.1>
- Servais, J. W., Choi, S. H., Sharp, W. D., Ross, J., Zoglman-Schuman, M., & Mukasa, S. B. (2011). Serpentinite matrix melange: Implications of mixed provenance for melange formation. *Geological Society of America Special Paper*, 480, 1–30. [https://doi.org/10.1130/2011.2480\(01\)](https://doi.org/10.1130/2011.2480(01))
- Servais, J. W., & Hanan, B. B. (1989). Jurassic volcanic glass from the Stonyford volcanic complex, Franciscan assemblage, northern California Coast Ranges. *Geology*, 17(6), 510. [https://doi.org/10.1130/0091-7613\(1989\)017<0510:JVGFST>2.3.CO;2](https://doi.org/10.1130/0091-7613(1989)017<0510:JVGFST>2.3.CO;2)
- Servais, J. W., & Kimbrough, D. L. (1985a). Geochemical evidence for the tectonic setting of the Coast Range ophiolite: A composite island arc–oceanic crust terrane in western California. *Geology*, 13(1), 35. [https://doi.org/10.1130/0091-7613\(1985\)13<35:GEFTTS>2.0.CO;2](https://doi.org/10.1130/0091-7613(1985)13<35:GEFTTS>2.0.CO;2)
- Servais, J. W., & Kimbrough, D. L. (1985b). Reply on “Geochemical evidence for the tectonic setting of the Coast Range ophiolite: A composite island arc–oceanic crust terrane in western California”. *Geology*, 13(11), 827. [https://doi.org/10.1130/0091-7613\(1985\)13<827:CAROGE>2.0.CO;2](https://doi.org/10.1130/0091-7613(1985)13<827:CAROGE>2.0.CO;2)
- Servais, J. W., & Kimbrough, D. L. (1987). Alkaline and transitional subalkaline metabasalts in the Franciscan Complex mélange, California. In *Geological Society of America Special Papers* (pp. 165–182). Geological Society of America. <https://doi.org/10.1130/SPE215-p165>
- Servais, J. W., Kimbrough, D. L., Renne, P., Hanan, B. B., Murchey, B., Snow, C. A., et al. (2004). Multi-stage origin of the Coast Range Ophiolite, California: Implications for the life cycle of supra-subduction zone ophiolites. *International Geology Review*, 46(4), 289–315. <https://doi.org/10.2747/0020-6814.46.4.289>
- Servais, J. W., Murchey, B. L., Kimbrough, D. L., Renne, P. R., & Hanan, B. (2005). Radioisotopic and biostratigraphic age relations in the Coast Range Ophiolite, northern California: Implications for the tectonic evolution of the Western Cordillera. *Geological Society of America Bulletin*, 117(5), 633. <https://doi.org/10.1130/B25443.1>
- Servais, J. W., Zoglman Schuman, M. M., & Hanan, B. B. (2005). The Stonyford volcanic complex: A forearc seamount in the Northern California Coast Ranges. *Journal of Petrology*, 46(10), 2091–2128. <https://doi.org/10.1093/petrology/egi048>
- Shreve, R. L., & Cloos, M. (1986). Dynamics of sediment subduction, melange formation, and prism accretion. *Journal of Geophysical Research*, 91(B10), 10229–10245. <https://doi.org/10.1029/JB091iB10p10229>
- Sibson, R. H. (2004). Controls on maximum fluid overpressure defining conditions for mesozonal mineralisation. *Journal of Structural Geology*, 26(6–7), 1127–1136. <https://doi.org/10.1016/j.jsg.2003.11.003>
- Sliter, W. V. (1984). Foraminifers from Cretaceous limestone of the Franciscan Complex, northern California. In *Franciscan Geology of Northern California, Pacific Section SEPM* (pp. 5–22).
- Sliter, W. V., & McGann, M. L. (1992). Age and correlation of the Calera limestone in the Permanente Terrane of northern California. *US Geological Survey Open File Report 92-0306* 27.
- Soret, M., Agard, P., Dubacq, B., Plunder, A., & Yamato, P. (2017). Petrological evidence for stepwise accretion of metamorphic soles during subduction infancy (Semail ophiolite, Oman and UAE). *Journal of Metamorphic Geology*, 35(9), 1051–1080. <https://doi.org/10.1111/jmg.12267>
- Soret, M., Agard, P., Ildefonse, B., Dubacq, B., Prigent, C., & Rosenberg, C. (2019). Deformation mechanisms in mafic amphibolites and granulites: Record from the Semail metamorphic sole during subduction infancy. *Solid Earth*, 10(5), 1733–1755. <https://doi.org/10.5194/se-10-1733-2019>
- Soret, M., Bonnet, G., Agard, P., Larson, K. P., Cottle, J. M., Dubacq, B., et al. (2022). Timescales of subduction initiation and evolution of subduction thermal regimes. *Earth and Planetary Science Letters*, 584, 117521. <https://doi.org/10.1016/j.epsl.2022.117521>
- Staudigel, H., & Clague, D. (2010). The geological history of deep-sea volcanoes. *Oceanography*, 23(01), 58–71. <https://doi.org/10.5670/oceanog.2010.62>
- Stern, R. J., Reagan, M., Ishizuka, O., Ohara, Y., & Whattam, S. A. (2012). To understand subduction initiation, study forearc crust: To understand forearc crust, study ophiolites. *Lithosphere*, 4(6), 469–483. <https://doi.org/10.1130/L183.1>
- Sun, S.-S., & McDonough, W. F. (1989). Chemical and isotopic systematics of oceanic basalts: Implications for mantle composition and processes. *Geological Society, London, Special Publications*, 42(1), 313–345. <https://doi.org/10.1144/GSL.SP.1989.042.01.19>
- Tagami, T., & Dumitru, T. A. (1996). Provenance and thermal history of the Franciscan accretionary complex: Constraints from zircon fission track thermochronology. *Journal of Geophysical Research*, 101(B5), 11353–11364. <https://doi.org/10.1029/96JB00407>
- Tan, Z., Agard, P., Gao, J., John, T., Li, J.-L., Jiang, T., et al. (2017). P–T–time–isotopic evolution of coesite-bearing eclogites: Implications for exhumation processes in SW Tianshan. *Lithos*, 278–281, 1–25. <https://doi.org/10.1016/j.lithos.2017.01.010>
- Tarduno, J. A., McWilliams, M., Debiche, M. G., Sliter, W. V., & Blake, M. C. (1985). Franciscan Complex Calera limestones: Accreted remnants of Farallon Plate oceanic plateaus. *Nature*, 317(6035), 345–347. <https://doi.org/10.1038/317345a0>
- Terabayashi, M., & Maruyama, S. (1998). Large pressure gap between the Coastal and Central Franciscan belts, northern and central California. *Tectonophysics*, 285(1–2), 87–101. [https://doi.org/10.1016/S0040-1951\(97\)00194-7](https://doi.org/10.1016/S0040-1951(97)00194-7)
- Tsujimori, T., Matsumoto, K., Wakabayashi, J., & Liou, J. G. (2006). Franciscan eclogite revisited: Reevaluation of the P–T evolution of tectonic blocks from Tiburon Peninsula, California, U.S.A. *Mineralogy and Petrology*, 88(1–2), 243–267. <https://doi.org/10.1007/s00710-006-0157-1>

- Ukar, E., & Cloos, M. (2015). Magmatic origin of low-T mafic blueschist and greenstone blocks from the Franciscan mélangé, San Simeon, California. *Lithos*, 230, 17–29. <https://doi.org/10.1016/j.lithos.2015.05.002>
- Ulmer, P., & Trommsdorff, V. (1995). Serpentine Stability to mantle depths and subduction-related magmatism. *Science*, 268(5212), 858–861. <https://doi.org/10.1126/science.268.5212.858>
- Van Andel, T. H. (1975). Mesozoic/cenozoic calcite compensation depth and the global distribution of calcareous sediments. *Earth and Planetary Science Letters*, 26(2), 187–194. [https://doi.org/10.1016/0012-821X\(75\)90086-2](https://doi.org/10.1016/0012-821X(75)90086-2)
- Wakabayashi, J. (1990). Counterclockwise *P-T-t* paths from amphibolites, Franciscan Complex, California: Relics from the early stages of subduction zone metamorphism. *The Journal of Geology*, 98(5), 657–680. <https://doi.org/10.1086/629432>
- Wakabayashi, J. (1999). Distribution of displacement on and evolution of a young transform fault system: The northern San Andreas fault system, California. *Tectonics*, 18(6), 1245–1274. <https://doi.org/10.1029/1999TC900049>
- Wakabayashi, J. (2015). Anatomy of a subduction complex: Architecture of the Franciscan Complex, California, at multiple length and time scales. *International Geology Review*, 57(5–8), 37–41. <https://doi.org/10.1080/00206814.2014.998728>
- Wakabayashi, J. (2017a). Sedimentary serpentinite and chaotic units of the lower Great Valley Group forearc basin deposits, California: Updates on distribution and characteristics. *International Geology Review*, 59(5–6), 599–620. <https://doi.org/10.1080/00206814.2016.1219679>
- Wakabayashi, J. (2017b). Structural context and variation of ocean plate stratigraphy, Franciscan Complex, California: Insight into mélangé origins and subduction-accretion processes. *Progress in Earth and Planetary Science*, 4(1), 18. <https://doi.org/10.1186/s40645-017-0132-y>
- Wakabayashi, J. (2021). Subduction and exhumation slip accommodation at depths of 10–80 km inferred from field geology of exhumed rocks: Evidence for temporal-spatial localization of slip. In J. Wakabayashi, Y. Dilek, & J. Wakabayashi (Eds.), *Plate Tectonics, Ophiolites, and Societal Significance of Geology: A Celebration of the Career of Eldridge Moores* (pp. 257–296). Geological Society of America. [https://doi.org/10.1130/2021.2552\(12\)](https://doi.org/10.1130/2021.2552(12))
- Wakabayashi, J., & Dilek, Y. (2000). Spatial and temporal relationships between ophiolites and their metamorphic soles: A test of models of forearc ophiolite genesis. *Geological Society of America Special Paper*, 349, 53–64. <https://doi.org/10.1130/0-8137-2349-3.53>
- Wakabayashi, J., & Dumitru, T. A. (2007). Ar ages from coherent, high-pressure metamorphic rocks of the Franciscan Complex, California: Revisiting the timing of metamorphism of the world's type subduction complex. *International Geology Review*, 49(10), 873–906. <https://doi.org/10.2747/0020-6814.49.10.873>
- Wakabayashi, J., Ghatak, A., & Basu, A. R. (2010). Suprasubduction-zone ophiolite generation, emplacement, and initiation of subduction: A perspective from geochemistry, metamorphism, geochronology, and regional geology. *Geological Society of America Bulletin*, 122(9–10), 1548–1568. <https://doi.org/10.1130/B30017.1>
- Wakabayashi, J., & Shimabukuro, D. H. (2022). The contrasting geologic record of inferred “hot” intraoceanic and “cold” continental margin subduction initiation. In C. Koeberl, P. Claeys, & A. Montanari (Eds.), *From the Guajira Desert to the Apennines, and from Mediterranean Microplates to the Mexican Killer Asteroid: Honoring the Career of Walter Alvarez* (pp. 169–194). Geological Society of America. [https://doi.org/10.1130/2022.2557\(11\)](https://doi.org/10.1130/2022.2557(11))
- Wan, B., Wang, X., Liu, X., Cai, K., Xiao, W., & Mitchell, R. N. (2021). Long-lived seamount subduction in ancient orogens: Evidence from the Paleozoic South Tianshan. *Geology*, 49(5), 531–535. <https://doi.org/10.1130/G48547.1>
- Wang, K., & Bilek, S. L. (2011). Do subducting seamounts generate or stop large earthquakes? *Geology*, 39(9), 819–822. <https://doi.org/10.1130/G31856.1>
- Watson, E. B., & Liang, Y. (1995). A simple model for sector zoning in slowly grown crystals; implications for growth rate and lattice diffusion, with emphasis on accessory minerals in crustal rocks. *American Mineralogist*, 80(11–12), 1179–1187. <https://doi.org/10.2138/am-1995-11-1209>
- Watts, A. B., Koppers, A., & Robinson, D. P. (2010). Seamount subduction and earthquakes. *Oceanography*, 23(01), 166–173. <https://doi.org/10.5670/oceanog.2010.68>
- Wessel, P., Sandwell, D. T., & Kim, S.-S. (2010). The Global Seamount Census. *Oceanography*, 23(01), 24–33. <https://doi.org/10.5670/oceanog.2010.60>
- Wood, D. A. (1980). The application of a Th-Hf-Ta diagram to problems of tectonomagmatic classification and to establishing the nature of crustal contamination of basaltic lavas of the British Tertiary Volcanic Province. *Earth and Planetary Science Letters*, 50(1), 11–30. [https://doi.org/10.1016/0012-821X\(80\)90116-8](https://doi.org/10.1016/0012-821X(80)90116-8)
- York, D. (1967). The best isochron. *Earth and Planetary Science Letters*, 2(5), 479–482. [https://doi.org/10.1016/0012-821X\(67\)90193-8](https://doi.org/10.1016/0012-821X(67)90193-8)

References From the Supporting Information

- Aleinikoff, J. N., Wintsch, R. P., Tollo, R. P., Unruh, D. M., Fanning, C. M., & Schmitz, M. D. (2007). Ages and origins of rocks of the Killington dome, south-central Connecticut: Implications for the tectonic evolution of southern New England. *American Journal of Science*, 307(1), 63–118. <https://doi.org/10.2475/01.2007.04>
- Connolly, J. A. D. (2005). Computation of phase equilibria by linear programming: A tool for geodynamic modeling and its application to subduction zone decarbonation. *Earth and Planetary Science Letters*, 236(1–2), 524–541. <https://doi.org/10.1016/j.epsl.2005.04.033>
- Connolly, J. A. D. (2009). The geodynamic equation of state: What and how. *Geochemistry, Geophysics, Geosystems*, 10(10), Q10014. <https://doi.org/10.1029/2009GC002540>
- Droop, G. T. R. (1987). A general equation for estimating Fe³⁺ concentrations in ferromagnesian silicates and oxides from microprobe analyses, using stoichiometric criteria. *Mineralogical Magazine*, 51(361), 431–435. <https://doi.org/10.1180/minmag.1987.051.361.10>
- Dumitru, T. A., Hourigan, J. K., Elder, W. P., Ernst, W. G., & Joesten, R. (2018). New, much younger ages for the Yolla Bolly terrane and a revised time line for accretion in the Franciscan subduction complex, California. In R. V. Ingersoll, T. F. Lawton, & S. A. Graham (Eds.), *Tectonics, Sedimentary Basins, and Provenance: A Celebration of the Career of William R. Dickinson*. Geological Society of America. [https://doi.org/10.1130/2018.2540\(15\)](https://doi.org/10.1130/2018.2540(15))
- Fuhrman, M. L., & Lindsley, D. H. (1988). Ternary-feldspar modeling and thermometry. *American Mineralogist*, 73, 201–215.
- Green, E. C. R., White, R. W., Diener, J. F. A., Powell, R., Holland, T. J. B., & Palin, R. M. (2016). Activity-composition relations for the calculation of partial melting equilibria in metabasic rocks. *Journal of Metamorphic Geology*, 34(9), 845–869. <https://doi.org/10.1111/jmg.1221>
- Holland, T. J. B., & Powell, R. (2011). An improved and extended internally consistent thermodynamic dataset for phases of petrological interest, involving a new equation of state for solids. *Journal of Metamorphic Geology*, 29(3), 333–383. <https://doi.org/10.1111/j.1525-1314.2010.00923.x>

- Horstwood, M. S. A., Košler, J., Gehrels, G., Jackson, S. E., McLean, N. M., Paton, C., et al. (2016). Community-derived standards for LA-ICP-MS U-(Th)-Pb geochronology – Uncertainty propagation, age interpretation and data reporting. *Geostandards and Geoanalytical Research*, 40(3), 311–332. <https://doi.org/10.1111/j.1751-908X.2016.00379.x>
- Jackson, S. E., Pearson, N. J., Griffin, W. L., & Belousova, E. A. (2004). The application of laser ablation-inductively coupled plasma-mass spectrometry to in situ U–Pb zircon geochronology. *Chemical Geology*, 211(1–2), 47–69. <https://doi.org/10.1016/j.chemgeo.2004.06.017>
- Jochum, K. P., Weis, U., Stoll, B., Kuzmin, D., Yang, Q., Raczek, I., et al. (2011). Determination of reference values for NIST SRM 610-617 glasses following ISO guidelines. *Geostandards and Geoanalytical Research*, 35(4), 397–429. <https://doi.org/10.1111/j.1751-908X.2011.00120.x>
- Kylander-Clark, A. R. C., Hacker, B. R., & Cottle, J. M. (2013). Laser-ablation split-stream ICP petrochronology. *Chemical Geology*, 345, 99–112. <https://doi.org/10.1016/j.chemgeo.2013.02.019>
- Leake, B. E., Wolley, A. R., Arps, C. E. S., Birch, W. D., Gilbert, M. C., Grice, J. D., et al. (1997). Nomenclature of amphiboles: Report of the Subcommittee on Amphiboles of the International Mineralogical Association, Commission on New Minerals and Mineral Names. *The Canadian Mineralogist*, 35, 219–246.
- Nemchin, A. A., & Cawood, P. A. (2005). Discordance of the U–Pb system in detrital zircons: Implication for provenance studies of sedimentary rocks. *Sedimentary Geology*, 182(1–4), 143–162. <https://doi.org/10.1016/j.sedgeo.2005.07.011>
- Paton, C., Hellstrom, J., Paul, B., Woodhead, J., & Hergt, J. (2011). Lolite: Freeware for the visualisation and processing of mass spectrometric data. *Journal of Analytical Atomic Spectrometry*, 26(12), 2508. <https://doi.org/10.1039/c1ja10172b>
- Powell, R., & Holland, T. J. B. (1994). Optimal geothermometry and geobarometry. *American Mineralogist*, 79(1–2), 120–133.
- Schmitz, M. D., & Bowring, S. A. (2001). U–Pb zircon and titanite systematics of the Fish Canyon Tuff: An assessment of high-precision U–Pb geochronology and its application to young volcanic rocks. *Geochimica et Cosmochimica Acta*, 65(15), 2571–2587. [https://doi.org/10.1016/S0016-7037\(01\)00616-0](https://doi.org/10.1016/S0016-7037(01)00616-0)
- Schmitz, M. D., & Schoene, B. (2007). Derivation of isotope ratios, errors, and error correlations for U–Pb geochronology using ^{205}Pb - ^{235}U -(^{233}U)-spiked isotope dilution thermal ionization mass spectrometric data. *Geochemistry, Geophysics, Geosystems*, 8(8), Q08006. <https://doi.org/10.1029/2006GC001492>
- Sláma, J., Košler, J., Condon, D. J., Crowley, J. L., Gerdes, A., Hanchar, J. M., et al. (2008). Plešovice zircon — A new natural reference material for U–Pb and Hf isotopic microanalysis. *Chemical Geology*, 249(1–2), 1–35. <https://doi.org/10.1016/j.chemgeo.2007.11.005>
- Spandler, C., Hammerli, J., Sha, P., Hilbert-Wolf, H., Hu, Y., Roberts, E., & Schmitz, M. (2016). MKED1: A new titanite standard for in situ analysis of Sm–Nd isotopes and U–Pb geochronology. *Chemical Geology*, 425, 110–126. <https://doi.org/10.1016/j.chemgeo.2016.01.002>
- Spencer, K. J., Hacker, B. R., Kylander-Clark, A. R. C., Andersen, T. B., Cottle, J. M., Stearns, M. A., et al. (2013). Campaign-style titanite U–Pb dating by laser-ablation ICP: Implications for crustal flow, phase transformations and titanite closure. *Chemical Geology*, 341, 84–101. <https://doi.org/10.1016/j.chemgeo.2012.11.012>
- Stacey, J. S., & Kramers, J. D. (1975). Approximation of terrestrial lead isotope evolution by a two-stage model. *Earth and Planetary Science Letters*, 26(2), 207–221. [https://doi.org/10.1016/0012-821X\(75\)90088-6](https://doi.org/10.1016/0012-821X(75)90088-6)
- Vermeech, P. (2018). IsoplotR: A free and open toolbox for geochronology. *Geoscience Frontiers*, 9(5), 1479–1493. <https://doi.org/10.1016/j.gsf.2018.04.001>
- White, R. W., Powell, R., Holland, T. J. B., Johnson, T. E., & Green, E. C. R. (2014). New mineral activity-composition relations for thermodynamic calculations in metapelitic systems. *Journal of Metamorphic Geology*, 32(3), 261–286. <https://doi.org/10.1111/jmg.12071>
- Wiedenbeck, M., Allé, P., Corfu, F., Griffin, W. L., Meier, M., Oberli, F., et al. (1995). Three natural zircon standards for U–Th–Pb, Lu–Hf, trace elements and REE analyses. *Geostandards and Geoanalytical Research*, 19(1), 1–23. <https://doi.org/10.1111/j.1751-908X.1995.tb00147.x>